On the Modeling of Friction and Rolling in Flexible Multi-Body Systems*

O.A. Bauchau
Georgia Institute of Technology,
School of Aerospace Engineering.
Atlanta, Georgia, 30332, USA.

Abstract

This paper is concerned with the dynamic analysis of flexible, nonlinear multi-body systems undergoing contact involving friction and rolling. A continuous friction law is used to model the friction forces between contacting bodies. This avoids the numerical problems associated with the discontinuity inherent to Coulomb's friction law and eliminates the need for different sets of equations modeling sliding and rolling as distinct phenomena. On the other hand, continuous friction laws eliminate specific physical phenomena implied by Coulomb's friction law. The condition of vanishing relative velocity between two contacting bodies is not possible: sticking or rolling are replaced by *creeping* with a small relative velocity. Discrete events such as transition from slipping to rolling or rolling to slipping are eliminated, together with the high frequency phenomena they are likely to cause. The computational issues associated with the continuous friction law and with the enforcement of the non-holonomic rolling constraint are addressed in this paper. This work is developed within the framework of energy preserving and decaying time integration schemes that provide unconditional stability for nonlinear, flexible multi-body systems undergoing contact involving friction and rolling.

1 Introduction

This paper is concerned with the dynamic analysis of flexible, nonlinear multi-body systems undergoing contact involving friction and rolling. Contact can occur between two rigid or deformable bodies of the system, or with an external body. The approaches to modeling of intermittent contact fall into two broad categories depending on the assumed duration of contact. In the first approach, contact is treated as a discontinuity, *i.e.* the duration of contact is assumed to tend to zero. The configuration of the system is assumed to be identical before and after impact, and the principle of impulse and momentum is used to compute the momenta after impact. Energy transfer during impact can be modeled in a heuristic

* *Multibody System Dynamics*, **3**, pp 209 – 239, 1999

manner using the concept of coefficient of restitution. This approach was first proposed by Kane [1], then applied to rigid multi-body systems by Haug and Wehage [2], and extended to flexible systems by Khulief and Shabana [3]. The accuracy of this approach is inherently limited by the assumption of a vanishing impact duration. Furthermore, energy balance is not necessarily satisfied when the principle of impulse and momentum is applied [4].

In the second approach, contact is of finite duration, and the time history of the forces acting between the contacting bodies which can be either rigid or deformable is explicitly computed during the simulation. Of course, a constitutive law describing the force-deformation relationship for the contacting bodies is required if the bodies are deformable. This approach was used by a number of researchers [5, 6, 7], among others. Various types of constitutive laws were used, but the classical solution of the static contact problem presented by Hertz [8] has been used by many investigators. Energy dissipation can be added in an appropriate manner, as proposed by Hunt and Crossley [9].

A methodology for the analysis of flexible multibody systems undergoing intermittent contacts of finite duration was developed in [10]. The overall approach is broken into three separate parts: a purely kinematic part describing the configuration of the contacting bodies, a unilateral contact condition, and an optional contact model. The first, purely kinematic part of the problem uses the concept of candidate contact points [11], *i.e.* the points of the bodies that are the most likely to come in contact if the bodies were in contact. These points are defined by a number of holonomic constraints that involve the kinematic variables defining the configuration of the contacting bodies and the parameters that describe the curve defining their outer shape. The knowledge of the location of these candidate contact points leads to the definition of the relative distance q between the bodies.

The second part of the model is the unilateral contact condition which is readily expressed in terms of the relative distance as $q \geq 0$. This condition is transformed into a holonomic constraint by the addition of a slack variable. For simple cases, this procedure yields a discrete version of the principle of impulse and momentum. The last part of the model is the contact model which takes into account the physical characteristics of the contacting bodies. This model consists of a constitutive law that describes the relationship between the normal contact force and the local inter-penetration of the bodies, called *approach*.

More often than not, friction will play an important role when two bodies come in contact. Friction is a phenomenon involving complex interaction mechanisms between the surfaces of solids being pressed into contact [12, 13]. Coulomb's friction law has been extensively used to model friction forces. It postulates that the friction force between to bodies sliding with respect to each other is equal to the normal contact force times an empirical coefficient μ_k, the *coefficient of kinetic friction*. The friction force always acts in a direction opposing relative motion. Sliding gives way to rolling or sticking when the relative velocity vanishes. In that case, the friction force must be smaller than the normal contact force times an empirical coefficient μ_s, the *coefficient of static friction*.

Computer simulations using Coulomb's friction law encounter numerical difficulties associated with the discontinuity of the friction force at zero relative velocity. Furthermore, the transition points from slipping to rolling or rolling to slipping must be accurately determined. Consequently, various approximations to Coulomb's law have been presented in the literature [14, 15, 16]; a comparison between these various models appears in [17]. Although based on different physical arguments, these various approximations can be viewed as *continuous*

friction laws that replace the discontinuity at zero relative velocity present in Coulomb's friction law by a smooth, rapidly varying function of the relative velocity. Various types of smoothing functions have been used by different authors [13, 18, 7, 19]. It is important to note that the continuous friction law replaces both kinetic and static friction laws.

The advantages of using a continuous friction law are clear. First, the numerical problems associated with the discontinuity inherent to Coulomb's friction law are avoided. Second, the need for different sets of equations modeling sliding and rolling as distinct phenomena is eliminated, and the accurate determination of the transition points is not required. On the other hand, continuous friction laws eliminate specific physical phenomena implied by Coulomb's friction law. The condition of vanishing relative velocity between two contacting bodies is not possible. Hence, sticking or rolling are replaced by *creeping* with a small relative velocity. Discrete events such as transition from slipping to rolling or rolling to slipping are eliminated, together with the high frequency phenomena they are likely to cause. The computational issues associated with the continuous friction law and with the enforcement of the rolling constraint will be addressed in this paper.

The discretization of the friction forces and the non-holonomic rolling constraint will be formulated within the framework of the energy preserving and decaying schemes introduced in [20, 21, 22, 23]. In these schemes, unconditional stability is achieved for nonlinear elastic multi-body systems by combining two features: an energy preservation or decay statement for the elastic bodies of the system, and the vanishing of the work done by the forces of constraint. The use of these unconditionally stable schemes is of particular importance in contact problems involving friction and rolling whose dynamic response is very complex due to the large, rapidly varying contact and friction forces applied to the system.

The paper is organized in the following manner. Section 2 presents the kinematic description of the contact problem, and Coulomb's classical friction law is reviewed in section 3. Sections 4 and 5 present the modeling of the friction forces and rolling constraint, respectively. Details of the computation strategy used in this work are discussed in section 6, and three numerical examples presented in section 7.

2 Contact kinematics

2.1 Kinematic conventions and notations

The kinematic description of bodies in their undeformed and deformed configurations will make use of three orthogonal triads. First, an inertial triad is used as a global reference for the system; it is denoted $\mathcal{S}_I$ with unit vectors $\vec{\imath}_1$, $\vec{\imath}_2$, and $\vec{\imath}_3$. A second triad $\mathcal{S}_0$, with unit vectors $\vec{e}_{01}$, $\vec{e}_{02}$, and $\vec{e}_{03}$ is attached to the body and defines its orientation in the reference configuration. Finally, a third triad $\mathcal{S}^*$ with unit vectors $\vec{e}_1$, $\vec{e}_2$, and $\vec{e}_3$ defines the orientation of the body in its deformed configuration.

Let $\vec{u}_0$ and $\vec{u}$ be the displacement vectors from $\mathcal{S}_I$ to $\mathcal{S}_0$, and $\mathcal{S}_0$ to $\mathcal{S}^*$, respectively, and $\mathbf{R}_0$ and $\mathbf{R}$ the rotation tensors from $\mathcal{S}_I$ to $\mathcal{S}_0$, and $\mathcal{S}_0$ to $\mathcal{S}^*$, respectively. In this work, all vector and tensor components are measured in either $\mathcal{S}_I$ or $\mathcal{S}^*$. For instance, the components of vector $\vec{u}$ measured in $\mathcal{S}_I$, and $\mathcal{S}^*$ will be denoted $\underline{u}$, and $\underline{u}^*$, respectively, and clearly

$$\underline{u}^* = R_0^T R^T \ \underline{u}. \tag{1}$$

Similarly, the components of tensor $\mathbf{R}$ measured $\mathcal{S}_I$, and $\mathcal{S}^*$ will be denoted R, and R^*, respectively. The skew-symmetric matrix formed with the components $\underline{u}$ will be denoted $\widetilde{u}$.

2.2 Contacting body geometry

Intermittent contact is considered between two bodies of the system whose external shapes are described by planar curves that will be defined by their Bézier [24] representation, as shown in fig. 1. The present work is limited to planar contact problems. A typical curve is defined in the body attached coordinate system $\mathcal{S}^*$. Let $\underline{p}^0$ be the components of the position vector of a point on the curve measured in $\mathcal{S}^*$. The derivatives of the position vector are

$$\underline{p}^1(\eta) = \frac{d\underline{p}^0}{d\eta}; \quad \underline{p}^2(\eta) = \frac{d^2\underline{p}^0}{d^2\eta}, \tag{2}$$

where $\eta \in [0,1]$ parameterizes the Bézier curve and can be viewed as a material coordinate along the curve. Note that $\underline{p}^1$ is not a unit tangent vector since η does not measure length along the curve. The unit tangent vector $\vec{t}$, and the external normal to the curve are then

$$\underline{t}(\eta) = \frac{\underline{p}^1}{|\underline{p}^1|}; \quad \underline{n}(\eta) = \underline{t} \times \underline{b}, \tag{3}$$

where $\underline{b}$ are the components of the vector normal to the plane of the curve.

2.3 Contacting pair geometry

The two bodies undergoing intermittent contact, denoted with superscripts $(.)^k$ and $(.)^l$, respectively, are depicted in fig. 1. The components $\underline{Z}^k$ of the position vector of a point on the curve defining the outer shape of body k are

$$\underline{Z}^k = \underline{u}_0^k + \underline{u}^k + (R^k R_0^k \ \underline{p}^{0k}). \tag{4}$$

A similar definition holds for the components $\underline{Z}^l$ of the position vector of a point on the curve defining the outer shape of body l. The points on the curves that are the natural candidates to come in contact are defined by the following two constraints [11]

$$(\underline{p}^{1kT} \ R_0^{kT} R^{kT}) \ \widetilde{b} \ (R^l R_0^l \ \underline{p}^{1l}) = 0; \tag{5}$$

$$(\underline{p}^{1kT} \ R_0^{kT} R^{kT}) \ \underline{Z} = 0. \tag{6}$$

The first constraint implies the orthogonality of the tangent to body k and the external normal to body l, whereas the second constraint expresses the orthogonality of the tangent to body k and the vector $\underline{Z} = \underline{Z}^l - \underline{Z}^k$ joining the two candidate points. These two nonlinear equations could be used to determine η^k and η^l, the parameters defining the positions of the candidate contact point on the two curves. Finally, the relative distance q between the two candidate contact points is readily found as the projection of vector $\underline{Z}$ on the external normal to body k

$$q = \frac{\underline{p}^{1kT}}{|\underline{p}^{1k}|} \ R_0^{kT} R^{kT} \ \widetilde{b} \ \underline{Z} = (\underline{t}^T \ R_0^{kT} R^{kT}) \ \widetilde{b} \ \underline{Z}. \tag{7}$$

Reference [10] details how the nonlinear holonomic constraints (4, 5, 6) and (7) can be enforced within the framework of the energy preserving and decaying schemes introduced in [21].

3 Coulomb's friction law

Coulomb's friction law postulates that if two bodies are sliding with respect to each other at a relative tangential velocity v_t, a friction force F^f acting in the tangential direction appears at the contact point, such that

$$F^f = -\mu_k(v_t)\ \mathrm{sign}(v_t)\ F^n, \tag{8}$$

where F^n is the positive normal contact force and $\mu_k(v_t)$ the coefficient of kinetic friction. Fig. 2 depicts the friction force as a function of the tangential velocity, for the simple case of a constant friction coefficient $\mu_k = 0.3$ and unit normal force $F^n = 1$. Sliding gives way to rolling or sticking when the relative velocity vanishes. In that case, the friction force is

$$F^f \leq \mu_s\ F^n, \tag{9}$$

where μ_s is the coefficient of static friction.

Coulomb's friction law presents a discontinuity of the friction force at zero relative velocity, as shown in fig. 2. This discontinuity causes numerical difficulties in computer simulations and hence, various approximations to Coulomb's law have been proposed in the literature [14, 15, 16, 17]. These various approximations can be viewed as *continuous friction laws* that replace the discontinuity at zero relative velocity by a smooth, rapidly varying function of the relative velocity. In this work, the following continuous friction law [25] will be used

$$F^f = -\mu_k(v_t)\ \mathrm{sign}(v_t)\ (1 - e^{-|v_t|/v_0})\ F^n, \tag{10}$$

where v_0 is a characteristic relative velocity typically chosen to be small compared to the maximum relative velocity encountered during the simulation. Fig. 2 shows the friction force corresponding to the continuous friction law for $v_0 = 0.5\ m/sec$. It is important to note that the continuous friction law replaces both kinetic and static friction laws.

4 Modeling friction forces

The inertial velocity of the material point that instantaneously coincides with the candidate contact point is found by taking a time derivative of eq. (4) while holding the curve parameter η^k constant, to find

$$\dot{\underline{Z}}^k = \dot{\underline{u}}^k + (\widetilde{R^k R_0^k\ \underline{p}^{0k}})^T\ \underline{\omega}^k, \tag{11}$$

where $\dot{()}$ denotes a derivative with respect to time, $\tilde{\omega}^k = \dot{R}^k R^{kT}$, and $\underline{\omega}^k$ is the angular velocity of body k. The relative velocity of the candidate contact points on each body then becomes

$$\underline{v}_r = \dot{\underline{Z}}^l - \dot{\underline{Z}}^k = [\dot{\underline{u}}^l + (\widetilde{R^l R_0^l\ \underline{p}^{0l}})^T\ \underline{\omega}^l] - [\dot{\underline{u}}^k + (\widetilde{R^k R_0^k\ \underline{p}^{0k}})^T\ \underline{\omega}^k]. \tag{12}$$

The component of relative velocity in the tangential direction is

$$v_t = \frac{(R^l R_0^l \ \underline{p}^{1l})^T}{|R^l R_0^l \ \underline{p}^{1l}|} \left\{ [\dot{\underline{u}}^l + (\widetilde{R^l R_0^l \ \underline{p}^{0l}})^T \ \underline{\omega}^l] - [\dot{\underline{u}}^k + (\widetilde{R^k R_0^k \ \underline{p}^{0k}})^T \ \underline{\omega}^k] \right\}. \tag{13}$$

In view of the constraints described in section 2.3, the tangents at the candidate contact points are parallel to each other but pointing in opposite directions, see fig. 1. Consequently, the tangential velocity writes

$$v_t = (R^k R_0^k \ \underline{t}^k)^T [\dot{\underline{u}}^k + (\widetilde{R^k R_0^k \ \underline{p}^{0k}})^T \ \underline{\omega}^k] + (R^l R_0^l \ \underline{t}^l)^T [\dot{\underline{u}}^l + (\widetilde{R^l R_0^l \ \underline{p}^{0l}})^T \ \underline{\omega}^l]. \tag{14}$$

Virtual changes in the tangential component of the relative position are found in a similar manner

$$\delta q_t = [\delta \underline{u}^{kT} + \underline{\delta\psi}^{kT} (\widetilde{R^k R_0^k \ \underline{p}^{0k}})] \ R^k R_0^k \ \underline{t}^k + [\delta \underline{u}^{lT} + \underline{\delta\psi}^{lT} (\widetilde{R^l R_0^l \ \underline{p}^{0l}})] \ R^l R_0^l \ \underline{t}^l, \tag{15}$$

where $\widetilde{\delta\psi}^k = \delta R^k \ R^{kT}$ expresses virtual changes in the orientation of body k. The virtual work done by the friction force now becomes

$$\delta \mathcal{W}^f = \delta q_t \ F^f. \tag{16}$$

The generalized friction forces $\underline{\mathcal{F}}^f$ are found by introducing (15) to find

$$\delta \mathcal{W}^f = \begin{bmatrix} \delta \underline{u}^k \\ \underline{\delta\psi}^k \\ \underline{\delta u}^l \\ \underline{\delta\psi}^l \end{bmatrix}^T \cdot \begin{bmatrix} F^f & R^k R_0^k \ \underline{t}^k \\ F^f & R^k R_0^k \ \widetilde{p^{0k}} \ \underline{t}^k \\ F^f & R^l R_0^l \ \underline{t}^l \\ F^f & R^l R_0^l \ \widetilde{p^{0l}} \ \underline{t}^l \end{bmatrix} = \begin{bmatrix} \delta \underline{u}^k \\ \underline{\delta\psi}^k \\ \underline{\delta u}^l \\ \underline{\delta\psi}^l \end{bmatrix}^T \cdot \underline{\mathcal{F}}^f. \tag{17}$$

This work is formulated within the framework of energy preserving schemes which combine two features: an energy preservation statement for the elastic bodies, and the vanishing of the work done by the forces of constraint. This results in exact preservation of the total energy for the nonlinear multi-body systems [21]. To ensure the stability of the time integration process in the presence of friction forces, it is necessary to prove that the work done by the discretized friction forces is always dissipative. The following discretization of the generalized friction forces is proposed

$$\underline{\mathcal{F}}_m^f = \begin{bmatrix} F_m^f & (I + \frac{\tilde{r}^k}{2}) \ R_i^k R_0^k \ \underline{t}_m^k \\ F_m^f & (I + \frac{\tilde{r}^k}{2}) \ R_i^k R_0^k \ \widetilde{p_m^{0k}} \ \underline{t}_m^k \\ F_m^f & (I + \frac{\tilde{r}^l}{2}) \ R_i^l R_0^l \ \underline{t}_m^l \\ F_m^f & (I + \frac{\tilde{r}^l}{2}) \ R_i^l R_0^l \ \widetilde{p_m^{0l}} \ \underline{t}_m^l \end{bmatrix}. \tag{18}$$

where F_m^f are the mid-point friction forces, $\underline{r}$ the components of the Rodrigues parameters used to measure the incremental rotations, see Appendix A, and

$$\underline{p}_m^0 = \frac{\underline{p}_f^0 + \underline{p}_i^0}{2}; \quad \underline{t}_m = \frac{1}{2}(\frac{\underline{p}_f^1}{|\underline{p}_f^1|} + \frac{\underline{p}_i^1}{|\underline{p}_i^1|}). \tag{19}$$

Subscripts $(.)_i$ and $(.)_f$ are used to indicate the value of a quantity at the initial time t_i and final time t_f of a time step of size Δt, respectively. The work done by the discretized friction forces is computed as follows

$$\frac{\Delta \mathcal{W}^f}{\Delta t} = F_m^f \left\{ \lfloor \underline{t}_m^{kT},\ \underline{t}_m^k\ \widetilde{p_m^{0k}}^T \rfloor\ (\mathcal{R}_0^{kT}\mathcal{R}_i^{kT} \begin{bmatrix} (I - \frac{\tilde{r}^k}{2})\frac{\underline{u}_f^k - \underline{u}_i^k}{\Delta t} \\ (I - \frac{\tilde{r}^k}{2})\frac{\underline{r}^k}{\Delta t} \end{bmatrix}) \right.$$
$$\left. + \lfloor \underline{t}_m^{lT},\ \underline{t}_m^l\ \widetilde{p_m^{0l}}^T \rfloor\ (\mathcal{R}_0^{lT}\mathcal{R}_i^{lT} \begin{bmatrix} (I - \frac{\tilde{r}^l}{2})\frac{\underline{u}_f^l - \underline{u}_i^l}{\Delta t} \\ (I - \frac{\tilde{r}^l}{2})\frac{\underline{r}^l}{\Delta t} \end{bmatrix}) \right\}. \tag{20}$$

Note that the two terms in parenthesis are the discretized mid-point velocities of bodies k and l. The work then becomes

$$\frac{\mathcal{W}^f}{\Delta t} = F_m^f\ v_{tm}, \tag{21}$$

where v_{tm} is the mid-point tangential velocity. Finally, introducing the continuous friction law (10) expressed at the mid-point yields

$$\frac{\mathcal{W}^f}{\Delta t} = -\mu_k(v_{tm})\ |v_{tm}|\ (1 - e^{-|v_{tm}|/v_0})\ F_m^n \leq 0, \tag{22}$$

where F_m^n is the mid point normal contact force. Inequality (22) guarantees energy dissipation in the presence of friction forces, and hence, establishes the numerical stability of the discrete time integration procedure in the presence of friction forces. Generalization to energy decaying schemes is straightforward by following the steps outlined in [21].

5 Modeling the rolling constraint

When two contacting bodies are rolling or sticking, their relative tangential velocity vanishes, and they exert on each other a friction force given by (9). The rolling or sticking constraint is $v_t = 0$, where v_t is given by (14). This corresponds to a non-holonomic constraint which writes

$$\mathcal{C} = [\delta \underline{u}^{kT} + \underline{\delta\psi}^{kT}(\widetilde{R^k R_0^k\ \underline{p}^{0k}})]\ R^k R_0^k\ \underline{t}^k + [\delta \underline{u}^{lT} + \underline{\delta\psi}^{lT}(\widetilde{R^l R_0^l\ \underline{p}^{0l}})]\ R^l R_0^l\ \underline{t}^l = 0. \tag{23}$$

As discussed in [21], constraints are enforced by the addition of a constraint potential $\lambda\ \mathcal{C}$, where λ is the Lagrange multiplier. The forces of constraint $\underline{\mathcal{F}}^c$ corresponding to the rolling constraint (23) are readily obtained as

$$\delta\mathcal{C} \cdot \lambda = \begin{bmatrix} \delta \underline{u}^k \\ \underline{\delta\psi}^k \\ \delta \underline{u}^l \\ \underline{\delta\psi}^l \end{bmatrix}^T \cdot \begin{bmatrix} \lambda & R^k R_0^k\ \underline{t}^k \\ \lambda & R^k R_0^k\ \widetilde{p^{0k}}\ \underline{t}^k \\ \lambda & R^l R_0^l\ \underline{t}^l \\ \lambda & R^l R_0^l\ \widetilde{p^{0l}}\ \underline{t}^l \end{bmatrix} = \begin{bmatrix} \delta \underline{u}^k \\ \underline{\delta\psi}^k \\ \delta \underline{u}^l \\ \underline{\delta\psi}^l \end{bmatrix}^T \cdot \underline{\mathcal{F}}^c. \tag{24}$$

To obtain unconditionally stable schemes for constrained systems, these forces of constraint must be discretized so that the work they perform vanishes exactly. The following discretization is proposed

$$\underline{\mathcal{F}}^c_m = \begin{bmatrix} s\lambda_m & (I + \frac{\tilde{r}^k}{2})\ R^k_i R^k_0\ \underline{t}^k_m \\ s\lambda_m & (I + \frac{\tilde{r}^k}{2})\ R^k_i R^k_0\ \widetilde{p^{0k}_m}\ \underline{t}^k_m \\ s\lambda_m & (I + \frac{\tilde{r}^l}{2})\ R^l_i R^l_0\ \underline{t}^l_m \\ s\lambda_m & (I + \frac{\tilde{r}^l}{2})\ R^l_i R^l_0\ \widetilde{p^{0l}_m}\ \underline{t}^l_m \end{bmatrix}, \tag{25}$$

where s is a scaling factor for the Lagrange multiplier, and λ_m the unknown mid-point value of this multiplier. The work done by these constraint forces is computed as follows

$$\frac{\Delta \mathcal{W}^f}{\Delta t} = s\lambda_m \left\{ \lfloor \underline{t}^{kT}_m,\ \underline{t}^k_m \widetilde{p^{0kT}_m} \rfloor\ (\mathcal{R}^{kT}_0 \mathcal{R}^{kT}_i \begin{bmatrix} (I - \frac{\tilde{r}^k}{2}) \frac{\underline{u}^k_f - \underline{u}^k_i}{\Delta t} \\ (I - \frac{\tilde{r}^k}{2}) \frac{\underline{r}^k}{\Delta t} \end{bmatrix}) \right.$$
$$\left. + \lfloor \underline{t}^{lT}_m,\ \underline{t}^l_m \widetilde{p^{0lT}_m} \rfloor\ (\mathcal{R}^{lT}_0 \mathcal{R}^{lT}_i \begin{bmatrix} (I - \frac{\tilde{r}^l}{2}) \frac{\underline{u}^l_f - \underline{u}^l_i}{\Delta t} \\ (I - \frac{\tilde{r}^l}{2}) \frac{\underline{r}^l}{\Delta t} \end{bmatrix}) \right\} = s\lambda_m\ v_{tm}. \tag{26}$$

It is now clear that the work done by the discretized constraint forces vanishes if $v_{tm} = 0$. In summary, discretization (25), together with the constraint $v_{tm} = 0$, leads to the vanishing of the work done by the forces of constraint. This energy preserving formulation can be readily extended to an energy decaying formulation by following the steps outlined in [21].

6 Computational strategy

The effective use of the continuous friction law (10) presents several challenges. Clearly, the characteristic velocity v_0 appearing in (10) must be carefully selected: if v_0 is too small, a near discontinuity is recovered, and if v_0 is too large, erroneous predictions will result because the value of the friction coefficient is incorrect over a wide range of relative velocities. In the numerical examples presented in section 7, the value of v_0 was set at about 1% of the maximum relative tangential velocity observed during the simulation.

To be fully effective, the continuous friction law must be used in conjunction with an automated time step size selection procedure. Indeed, as the norm of the relative velocity approaches v_0, a small enough time step size must be selected so that the subsequent changes in relative velocity are small compared to v_0. In this work, a simple strategy was used: when $|v_t|$ becomes smaller than $3v_0$, the time step size Δt_{new} for the next time step is selected in such a way that the estimated change in relative velocity $\Delta v_t \approx v_0/10$. A simple linear extrapolation based on the previous time step size Δt_{old} and corresponding relative velocity v_{told} was found to predict Δv_t with sufficient accuracy.

According to Coulomb's classical friction law, rolling starts when the relative velocity vanishes and condition (9) holds. In this work the rolling constraint (23) was enforced when

the relative velocity v_t becomes smaller than $v_0/2$. The Lagrange multiplier associated with this non-holonomic constraint is equal to the static friction force. The rolling constraint remains in force for as long as condition (9) holds. If it is no longer satisfied, the time step is rejected and restarted using the continuous friction law. The activation of the rolling constraint, *i.e.* the slipping to rolling transition, did not upset the time integration process. However, the de-activation of the constraint, *i.e.* the rolling to slipping transition, is more critical because a non vanishing relative velocity suddenly appears, corresponding to a large acceleration. If convergence failed, the time step size was halved until convergence was achieved.

An automated time step size selection procedure developed in [21] was used to obtain accurate solutions in an efficient manner. The error estimate used in the procedure is based on system total energy considerations. The smallest time step size required by the various adaptivity strategies was used to proceed with the simulation.

7 Numerical examples

7.1 Locking of a spring loaded pin in a slot

The first numerical example deals with the locking of a spring loaded pin in a slot as is depicted in fig. 3. As the beam rotates under the effect of the applied tip load, the spring loaded pin rotates in the locking mechanism which consists of a cavity with a deep slot. Due to friction forces, the pin is captured in the slot and locks the beam in a vertical position. The beam of length $L = 2.4\ m$ is pinned to the ground at point R by means of a revolute joint. The polar moment of inertia of the joint is $I_R = 0.02\ kg.m^2$. A rigid body of mass $M_A = 40.0\ kg$ and polar moment of inertia $I_A = 1.0\ kg.m^2$ is attached at the free end of the beam which is modeled with four cubic beam elements. The physical properties of the beam are given as the first set in table 1. A pin of length $l = 0.162\ m$ is connected to the revolute joint through a prismatic joint allowing axial motion of the pin. A spring of constant $k_s = 4.0\ kN/m$ and pre-stretched of $\Delta = -0.1\ m$ is located in the prismatic joint. The physical properties of the pin are given as the first set in table 1. The pin is modeled by two cubic beam elements and a rigid body is attached to its tip. This rigid body has a mass $M_B = 50.0\ g$, a polar moment of inertia $I_B = 1.0\ g.m^2$, and its outer shape is defined by a Bézier [24] curve which control polygon is defined in Table 2. The pin assembly is located inside a stationary cavity which inner shape is defined by a cubic B-spline [24] curve which control polygon is given in Table 3.

The simulation is started from the static equilibrium configuration of the preloaded pin contacting the cavity at point B. The contact forces are given by a linear model $F^n = c_0\ a$, where a is the approach, and $c_0 = 2.0\ GPa.m$. Two different simulations will be presented. *Case 0* is a reference case for which friction effects are neglected. For *case 1*, friction effects are modeled using the continuous friction law (10), with a kinetic friction coefficient $\mu_k = 0.30$, and $v_0 = 4.0\ mm/sec$. Rolling was not allowed. The beam is subjected to a tip vertical load $F(t)$ with the following schedule

$$F(t) = \begin{cases} 250\ (1 - \cos 2\pi t)\ N & t \leq 1\ sec; \\ 0 & t > 1\ sec. \end{cases}$$

Fig. 4 shows the beam tip displacement. In the absence of friction forces (*i.e. case 0*), the pin is not captured by the slot and the beam continues its counter-clockwise rotation. Hence, the simulation was stopped after 1.8 *sec*, at which time the beam has rotated by more than 180 degrees. For *case 1*, the friction forces cause the pin to remain in the slot and once captured, the beam oscillates back and forth about a vertical position. This behavior is best seen on fig. 5 which depicts the history of the location of the contact point. For *case 0*, the pin reaches the bottom of the slot at time $t \approx 1.2$ *sec* then rapidly clears the slot. For *case 1*, the pin first reaches the bottom of the slot at time $t \approx 1.6$ *sec* but does not clear the slot, returning to the bottom at times $t \approx 2.5$ and 3.5 *sec*.

The beam mid-point axial and shearing forces are depicted in fig. 6. The large axial force is due to the centrifugal effects associated with the angular velocity of the beam. The shear force presents a first peak as the pin is moving toward the slot, followed by two very high peaks resulting from the pin coming to a halt against the nearly vertical walls of the slot. Fig. 7 shows the beam mid-point bending moment. High frequency vibrations are observed for *case 0*, due to the absence of any energy dissipation mechanism. For *case 1*, high frequency vibrations appear after the first motion reversal due to the impulsive nature of this phenomenon.

The corresponding results for the pin mid-point forces, and bending moment are presented in figs. 8, and 9, respectively. Finally, fig. 10 shows the normal contact force. For *case 0* this contact force is approximately equal to the elastic force in the prismatic joint spring and remains small at all times. The contact forces for *case 1* are one order of magnitude larger than those observed in *case 0*, due to the large bending of the pin induced by the friction forces.

7.2 Locking mechanism

The second example deals with a locking mechanism consisting of a cam and a cantilevered beam, as shown in fig. 11. As the cam slowly rotates to a vertical position, it contacts the body placed at the beam mid-span. The upward thrust imparted by the cam on the beam creates elastic deformations and subsequent vibrations in the beam, resulting in contact involving a complex combination of friction and rolling. The beam has a length $L = 2.4\ m$; its physical properties are defined in the first set of table 1; and it is modeled with eight cubic beam elements. A rigid body of mass $M_T = 40\ kg$ is attached at its free end. Another rigid body with a mass $M_P = 4\ kg$ is attached at the beam mid-span location and the outer shape of this body is defined by a Bézier [24] curve which control polygon is defined in Table 4.

The cam is supported by a pinned beam of length $l = 0.3\ m$ and is modeled with two cubic beam elements. Its physical properties are defined in the second set of table 1. A rigid body with a mass $M_i = 4\ kg$ is attached at the beam tip and the outer shape of this body is defined by the Bézier control polygon given in Table 5. The angular motion of the cam is prescribed as

$$\Phi(t) = \begin{cases} 30^\circ(1 + \cos \pi t) & t \leq 1\ sec; \\ 0 & t > 1\ sec. \end{cases}$$

The contact forces are given by the Hertz model $F^n = c_1\ a^{3/2}$, where a is the approach, and $c_1 = 20.0\ GPa.\sqrt{m}$.

Three different simulations will be presented. *Case 0* is a reference case for which friction effects are neglected. For *case 1*, friction effects are modeled using the continuous friction law (10), with a kinetic friction coefficient $\mu_k = 0.30$, and $v_0 = 2.5\ mm/sec$. Rolling was not allowed. Finally, *case 2* is identical to *case 1*, except that the rolling constraint was imposed when the relative tangential velocity became smaller that $v_0/2$, and the coefficient of static friction was $\mu_s = 0.30$.

The tip- and mid-point transverse displacements of the beam are depicted in fig. 12. As the cam approaches the vertical position, the beam is pushed up. For times $t > 1\ sec$, the cam remains in the vertical position; the mid-span deflection remains nearly constant, whereas the beam tip oscillates due to dynamic effects. Predictions are in close agreement for all three cases, except that the friction forces in *cases 1* and *2* provide a damping mechanism that is absent in *case 0*. For times $t < 1\ sec$, a non vanishing relative tangential velocity results from the prescribed motion of the cam, no rolling occurs. For times $t > 1\ sec$, the relative motion and tangential velocity of the two bodies are driven by the beam's oscillations and remain small. The motion consists of a succession of 7 distinct rolling events separated by slipping. The extent of the rolling events is indicated by the thick horizontal lines appearing in fig. 12.

Fig. 13 shows the driving torque required to prescribe the desired motion of the cam. For times $t < 1\ sec$, the required torque is significantly higher for *cases 1* and *2* as compared to *case 0*, due to the presence of the friction force. For times $t > 1\ sec$, the torque settles to a nearly constant value of about $-1.0\ kN.m$ for *case 0*. This contrasts with the predictions for *cases 1* and *2* which exhibit large amplitude oscillations associated with the successive rolling and sliding events.

The bending moments at the root of the beam and cam are depicted in fig. 14. Fig. 15 shows the history of the normal contact force. The results presented thus far show excellent correlation between *cases 1* and *2*, proving that the continuous friction law (10) is indeed capable of accurately modeling the present problem that involves rolling, although the rolling constraint is not explicitely enforced in *case 1*. However, the difference between *cases 1* and *2* is apparent in fig. 16 that depicts the work done by the friction forces. For *case 1*, the friction forces are dissipative even when the relative velocity becomes very small, whereas for *case 2*, the work done by the static friction force during the rolling events vanishes exactly, as implied by (26) together with the constraint $v_{tm} = 0$.

Another difference between *cases 1* and *2* is the required computational effort. Fig. 17 shows the history of the time step size during the simulation. During the rolling events, much smaller time steps are required for *case 1* because sharp variations in friction force are implied by the continuous friction law (10) at small relative velocities.

7.3 Cam contact with rolling

The last example deals with the interaction between two cams supported by elastic beams, as shown in fig. 18 which depicts the unstressed configurations of the beams. As the leftward motion of *beam B* is prescribed, the interaction between the two cams again involves friction and rolling. *Beam A* has a length $L_A = 1.1\ m$, is clamped at point L, and its physical properties are defined in the first set of table 1. A rigid body (*body A*), of mass $M_A = 4.0\ kg$ and polar moment of inertia $I_A = 0.02\ kg.m^2$ is rigidly connected to the free end of the

beam which is modeled with four cubic beam elements. The outer shape of the rigid body is defined by a Bézier [24] curve which control polygon is defined in Table 6.

Beam B has a length $L_B = 1.2\ m$ and is connected to a prismatic joint at point R. At point B, it is attached to a rigid body (*body B*) by means of a revolute joint including a torsional spring of constant $k_s = 10^{+12}\ N.m/rad$, *i.e.* the rigid body is clamped to the tip of the beam. The two beams have identical physical properties and mesh, and the the two rigid bodies are mirror images of one another, as shown in fig. 18. There is an offset $d = 0.1\ m$ between the axes of the two beams. The configuration shown in fig. 18 corresponds to the unstressed position of the beams. All simulations were started from the equilibrium state of the system when both cams are in contact at a point. The contact forces are given by the Hertz model $F^n = c_1\ a^{3/2}$, where a is the approach, and $c_1 = 20.0\ GPa.\sqrt{m}$. The relative displacement $\Delta(t)$ of the prismatic joint is prescribed as follows

$$\Delta(t) = \begin{cases} 0.14\ (1 - \cos 4\pi t)\ m & t \leq 0.25\ sec; \\ 0 & t > 0.25\ sec. \end{cases}$$

Three different simulations will be presented. *Case 0* is a reference case for which friction effects are neglected. For *case 1*, friction effects are modeled using the continuous friction law (10), with a kinetic friction coefficient $\mu_k = 0.30$, and $v_0 = 4.0\ mm/sec$. Rolling was not allowed. Finally, *case 2* is identical to *case 1*, except that the rolling constraint was imposed when the relative tangential velocity became smaller that $v_0/2$, and the coefficient of static friction was $\mu_s = 0.30$.

Fig. 19 shows the transverse displacements of *beams A* and *B* which are near mirror images of each other as the two beam slide past each other. The predictions are nearly identical for all three cases. The motion involves both sliding and rolling, and the extent of the rolling events is indicated by the thick horizontal lines appearing in fig. 19. Note the very short (0.005 *sec*) rolling event at the beginning of the simulation, and the extensive rolling event from time $t = 0.35\ sec$ to the end of the simulation. The driving force required to prescribe the desired motion of *beam B* is depicted in fig. 20. Much lower forces a observed for *case 0* since there are no friction forces to overcome. *Cases 1* and *2* are in close agreement up to time $t = 0.35\ sec$, at which time rolling starts for *case 2*. If rolling is allowed (*case 2*), the friction force remains nearly constant, and so does the driving force. On the other hand, if rolling is not allowed (*case 1*), the driving force slowly decreases and asymptotically reaches *case 0* predictions. In analogy to material constitutive behavior, this phenomenon corresponds to the relaxation of internal stresses (friction forces): after an infinite relaxation time, the system comes back to a stress (friction forces) free state. This clearly underlines a shortcoming of the continuous friction law (10) which is unable to properly deal with the present rolling situation.

The normal contact force is depicted in fig. 21. Here again, the differences between *cases 1* and *2* discussed in the previous paragraph are apparent. Fig. 22 shows the point of contact material coordinate η on *bodies A* and *B*. Note the nearly identical results obtained for all threes *cases*. Indeed, rolling or relaxation of the friction forces occur with minute relative motions, although their effects on internal forces is significant, as shown in fig. 20.

A second set of simulations was run with a torsional spring of constant $k_s = 50\ N.m/rad$ for torsional spring in the revolute joint at point B. *Body B* is now virtually free to rotate about the tip of *beam B*. The transverse displacements of *beams A* and *B* are shown in fig. 23.

Here again the motion involves both sliding and rolling, and the extent of the rolling event is indicated by the thick horizontal line appearing in fig. 23. Rolling occurs from the beginning of the simulation up to a time $t \approx 0.15$ *sec*. The rotation of *body B* is depicted in fig. 24. For *cases 1* and *2*, *body B* rotates by more than 180 degrees, whereas a rotation of 70 degrees is predicted for *case 0*. This discrepancy is readily explained by the absence of friction forces in *case 0*. As the rotation of *body B* increase, a point is reached when Coulomb's static friction condition (9) is no longer satisfied, and sliding starts. This results in an oscillatory motion of *body B* that is rapidly damped by the friction forces.

The driving force required to prescribe the desired motion of *beam B* is depicted in fig. 25. Lower forces a observed for *case 0* since there are no friction forces to overcome. In fact, the driving force for *case 0* becomes negative due to the relative orientations of *bodies A* and *B* after the rotation of *body B* has taken place. For *case 1* and *2*, note the rapid drop in driving force after the onset of slipping and the nearly zero value of the final driving force.

The normal contact force is depicted in fig. 26. Although similar force levels are predicted in all three cases, note the high frequency content of the response for *cases 1* and *2*. Fig. 27 shows the point of contact material coordinate η on *bodies A* and *B*.

8 Conclusions

This paper has presented an analysis methodology for nonlinear, flexible multi-body systems undergoing contact involving friction and rolling. A continuous friction law was used to model the friction forces between contacting bodies and a procedure for the enforcement of the rolling constraint was described.

Although continuous friction laws are presumably capable of dealing with both slipping and rolling, the numerical examples presented in this paper have underlined their possible shortcomings. First and foremost, continuous friction laws can eliminate specific physical phenomena implied by Coulomb's friction law. The condition of vanishing relative velocity between two contacting bodies is not possible: sticking or rolling are replaced by *creeping* with a small relative velocity. Discrete events such as transition from slipping to rolling or rolling to slipping are eliminated, together with the high frequency phenomena they are likely to cause. Second, the small relative velocity present during rolling or sticking can burden the time integration process by requiring a time step size far smaller than would normally be required.

Consequently, it seems that friction effects in multi-body systems are best modeled through the combination of a continuous friction law working together with the enforcement of the rolling constraint. A computational strategy that coordinates these two aspects of the problem was proposed and its effectiveness demonstrated by means of several numerical examples. This work was developed within the framework of energy preserving and decaying time integration schemes that provide unconditional stability for nonlinear, flexible multi-body systems undergoing contact involving friction and rolling.

References

[1] T.R. Kane. Impulsive motions. *Journal of Applied Mechanics*, 15:718–732, 1962.

[2] E.J. Haug, R.A. Wehage, and N.C. Barman. Design sensitivity analysis of planar mechanisms and machine dynamics. *ASME Journal of Mechanical Design*, 103:560–570, 1981.

[3] Y.A. Khulief and A.A. Shabana. Dynamic analysis of constrained systems of rigid and flexible bodies with intermittent motion. *ASME Journal of Mechanisms, Transmissions, and Automation in Design*, 108:38–44, 1986.

[4] T.R. Kane. *Dynamics*. Holt, Rinehart and Winston, Inc, New York, 1968.

[5] Y.A. Khulief and A.A. Shabana. A continuous force model for the impact analysis of flexible multi-body systems. *Mechanism and Machine Theory*, 22:213–224, 1987.

[6] H.M. Lankarani and P.E. Nikravesh. A contact force model with hysteresis damping for impact analysis of multi-body systems. *Journal of Mechanical Design*, 112:369–376, 1990.

[7] A. Cardona and M. Géradin. Kinematic and dynamic analysis of mechanisms with cams. *Computer Methods in Applied Mechanics and Engineering*, 103:115–134, 1993.

[8] S.P. Timoshenko and J.M. Gere. *Theory of Elastic Stability*. McGraw-Hill, Inc., New York, 1961.

[9] K.H. Hunt and F.R.E. Crossley. Coefficient of restitution interpreted as damping in vibroimpact. *Journal of Applied Mechanics*, 112:440–445, 1975.

[10] O.A. Bauchau. Analysis of flexible multi-body systems with intermittent contacts. *Multibody System Dynamics*, 4:23–54, 2000.

[11] F. Pfeiffer and C. Glocker. *Multi-Body Dynamics with Unilateral Contacts*. John Wiley & Sons, Inc, New York, 1996.

[12] E. Rabinowicz. *Friction and Wear of Materials*. John Wiley & Sons, New York, second edition, 1995.

[13] J.C. Oden and J.A.C. Martins. Models and computational methods for dynamic friction phenomena. *Computer Methods in Applied Mechanics and Engineering*, 52:527–634, 1985.

[14] P.R. Dahl. Solid friction damping of mechanical vibrations. *AIAA Journal*, 14:1675–1682, 1976.

[15] T. Baumeister, E.A. Avallone, and T. Baumeister III (eds.). *Marks' Mechanical Engineers Handbook*. McGraw-Hill, Inc., New York, 1978.

[16] J.E. Shigley and C.R. Mischke. *Mechanical Engineering Design*. McGraw-Hill, Inc., New York, 1989.

[17] A.K. Banerjee and T.R. Kane. Modeling and simulation of rotor bearing friction. *Journal of Guidance, Control and Dynamics*, 17:1137–1151, 1994.

[18] A. Cardona, M. Géradin, and D.B. Doan. Rigid and flexible joint modelling in multibody dynamics using finite elements. *Computer Methods in Applied Mechanics and Engineering*, 89:395–418, 1991.

[19] P.C. Mitiguy and A.K. Banerjee. Efficient simulation of motions involving Coulomb friction. *Journal of Guidance, Control, and Dynamics*, 22:78–86, 1999.

[20] O.A. Bauchau and N.J. Theron. Energy decaying schemes for nonlinear elastic multibody systems. *Computers and Structures*, 59:317–331, 1996.

[21] O.A. Bauchau. Computational schemes for flexible, nonlinear multi-body systems. *Multibody System Dynamics*, 2:169–225, 1998.

[22] C.L. Bottasso and M. Borri. Energy preserving/decaying schemes for non-linear beam dynamics using the helicoidal approximation. *Computer Methods in Applied Mechanics and Engineering*, 143:393–415, 1997.

[23] C.L. Bottasso and M. Borri. Integrating finite rotations. *Computer Methods in Applied Mechanics and Engineering*, 164:307–331, 1998.

[24] G.E. Farin. *Curves and Surfaces for Computer Aided Geometric Design*. Academic Press, Inc., Boston, third edition, 1992.

[25] J. Srnik and F. Pfeiffer. Dynamics of CVT chain drives: Mechanical model and verification. In *Proceedings of the 16th Biennial Conference on Mechanical Vibration and Noise, Sacramento, CA, Sept. 14-17*, 1997.

[26] T.R. Kane and D.A. Levinson. *Dynamics: Theory and Applications*. McGraw-Hill, Inc., New York, 1985.

Appendix A Rodrigues parameters

A common representation of finite rotations [26] is in terms of Rodrigues parameters $\underline{r} = 2\underline{u}\ \tan\phi/2$, where ϕ is the magnitude of the finite rotation and $\underline{u}$ the components of the unit vector about which it takes place. The following notation is introduced

$$r_0 = \cos^2\frac{\phi}{2} = 1\ /\ (1 + \frac{\underline{r}^T\ \underline{r}}{4}), \tag{A1}$$

and the finite rotation tensor R then write

$$R(\underline{r}) = I + r_0\ \widetilde{r} + \frac{r_0}{2}\ \widetilde{r}\widetilde{r}. \tag{A2}$$

The relationship between angular velocities $\underline{\omega}$ and time derivatives of Rodrigues parameters is $\underline{\omega} = H\ \dot{\underline{r}}$, where

$$H(\underline{r}) = r_0(1 + \frac{1}{2}\ \widetilde{r}). \tag{A3}$$

The following two decompositions of the rotation tensor are extensively used in this work

$$R = HH^{-T} = H^{-T}H, \tag{A4}$$

and

$$R = \left(I + \frac{\tilde{r}}{2}\right)\left(I + \frac{\tilde{r}}{2}\right)^{-T} = \left(I + \frac{\tilde{r}}{2}\right)^{-T}\left(I + \frac{\tilde{r}}{2}\right). \tag{A5}$$

List of Tables

List of Figures

Property	Set 1	Set 2
Axial stiffness	44.0 MN	44.0 MN
Bending stiffness	23.0 $kN.m^2$	0.3 $MN.m^2$
Shearing stiffnesses	2.8 MN	14.0 MN
Mass per unit span	1.6 kg/m	1.6 kg/m
Mass moment of inertia	0.011 $kg.m$	0.011 $kg.m$

Table 1: Physical properties of the beams.

Control point	x_1 $[m]$	x_2 $[m]$	Control point	x_1 $[m]$	x_2 $[m]$
1	0.01	0.01	2	-0.01	0.04
3	-0.05	0.00	4	-0.01	-0.04
5	0.01	-0.01			

Table 2: Coordinates of the Bézier control polygon.

Control point	x_1 $[m]$	x_2 $[m]$	Control point	x_1 $[m]$	x_2 $[m]$
1	0.10	0.10	2	0.20	0.05
3	0.20	-0.05	4	0.04	-0.05
5	0.09	-0.15	6	-0.09	-0.15
7	-0.04	-0.05	8	-0.20	-0.05
9	-0.20	0.05	10	-0.10	0.10

Table 3: Coordinates of the cubic B-spline control polygon.

Control point	x_1 $[m]$	x_2 $[m]$	Control point	x_1 $[m]$	x_2 $[m]$
1	-0.1	0.2	2	-1.0	0.0
3	0.0	-0.3	4	1.0	0.0
5	0.1	0.2			

Table 4: Coordinates of the Bézier control polygon.

Control point	x_1 $[m]$	x_2 $[m]$	Control point	x_1 $[m]$	x_2 $[m]$
1	-0.025	-0.025	2	0.025	-0.1
3	0.125	0.0	4	0.025	0.1
5	-0.025	0.025			

Table 5: Coordinates of the Bézier control polygon.

Control point	x_1 $[m]$	x_2 $[m]$	Control point	x_1 $[m]$	x_2 $[m]$
1	-0.2	-0.1	2	0.0	-0.2
3	0.3	0.0	4	0.0	0.2
5	-0.2	0.1			

Table 6: Coordinates of the Bézier control polygon.

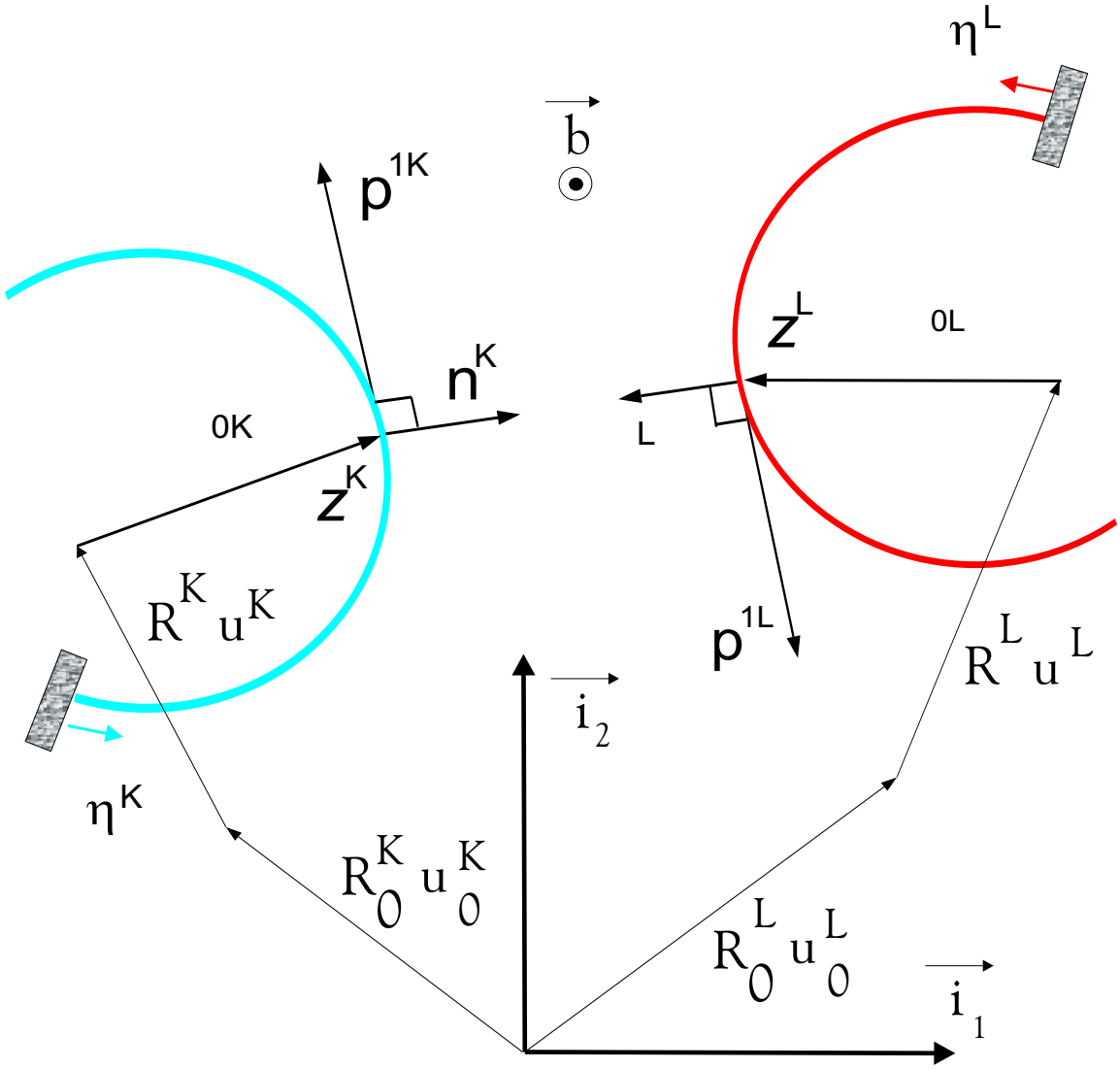

Figure 1: Geometry of the contacting bodies.

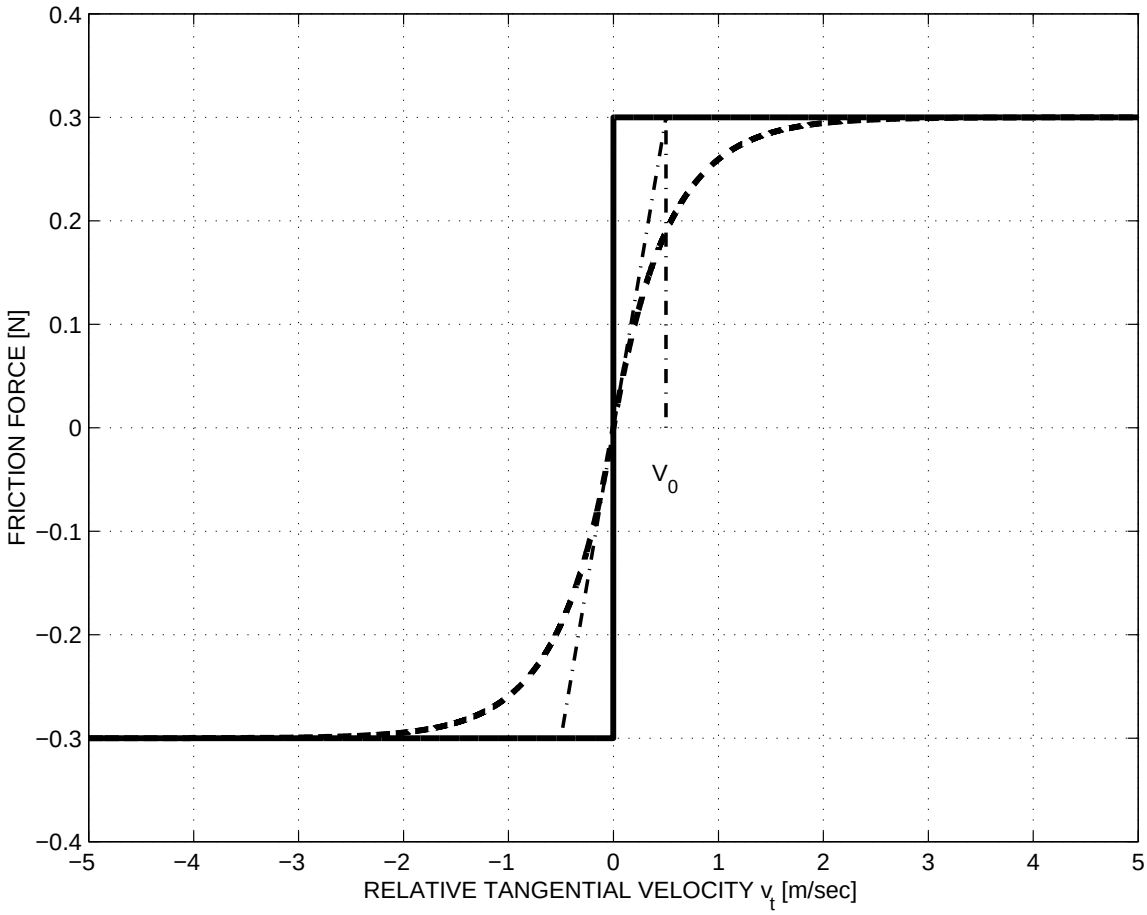

Figure 2: The friction force for Coulomb's friction law (solid line), and the continuous friction law (dashed line). $\mu_k = 0.3$; $F^n = 1$.

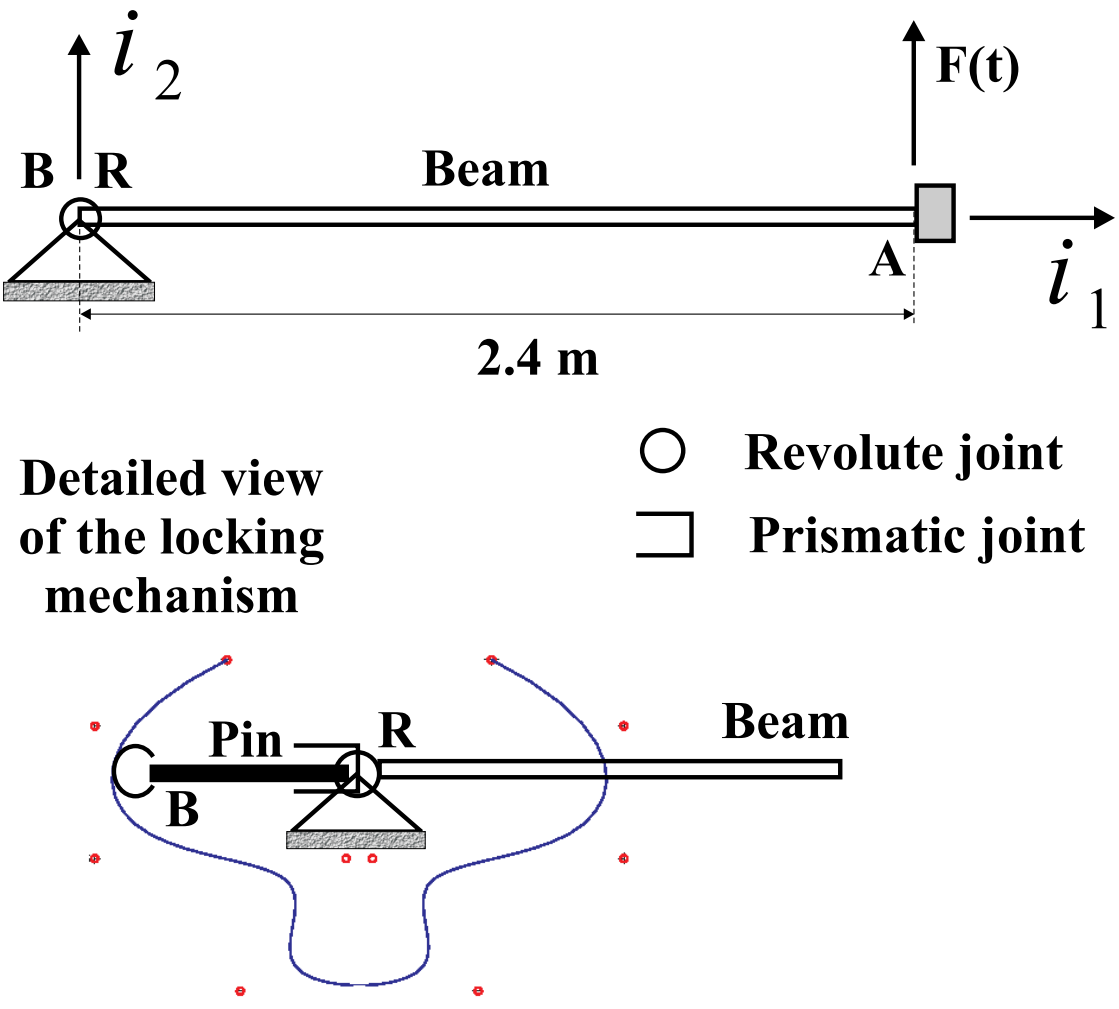

Figure 3: Configuration of the spring loaded pin and beam.

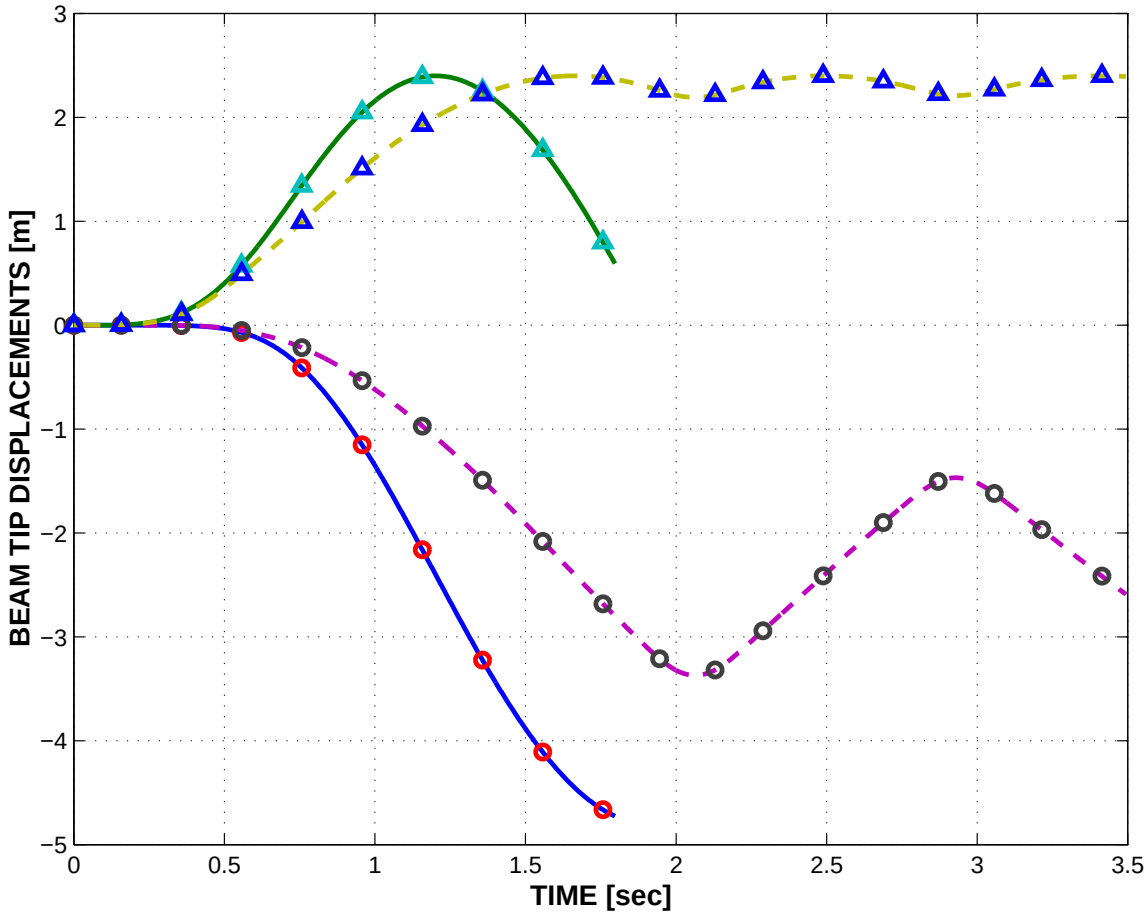

Figure 4: Time history of the beam tip u_1 ($\circ$) and u_2 ($\triangle$) displacement components. *Case 0:* solid line; *case 1:* dashed line.

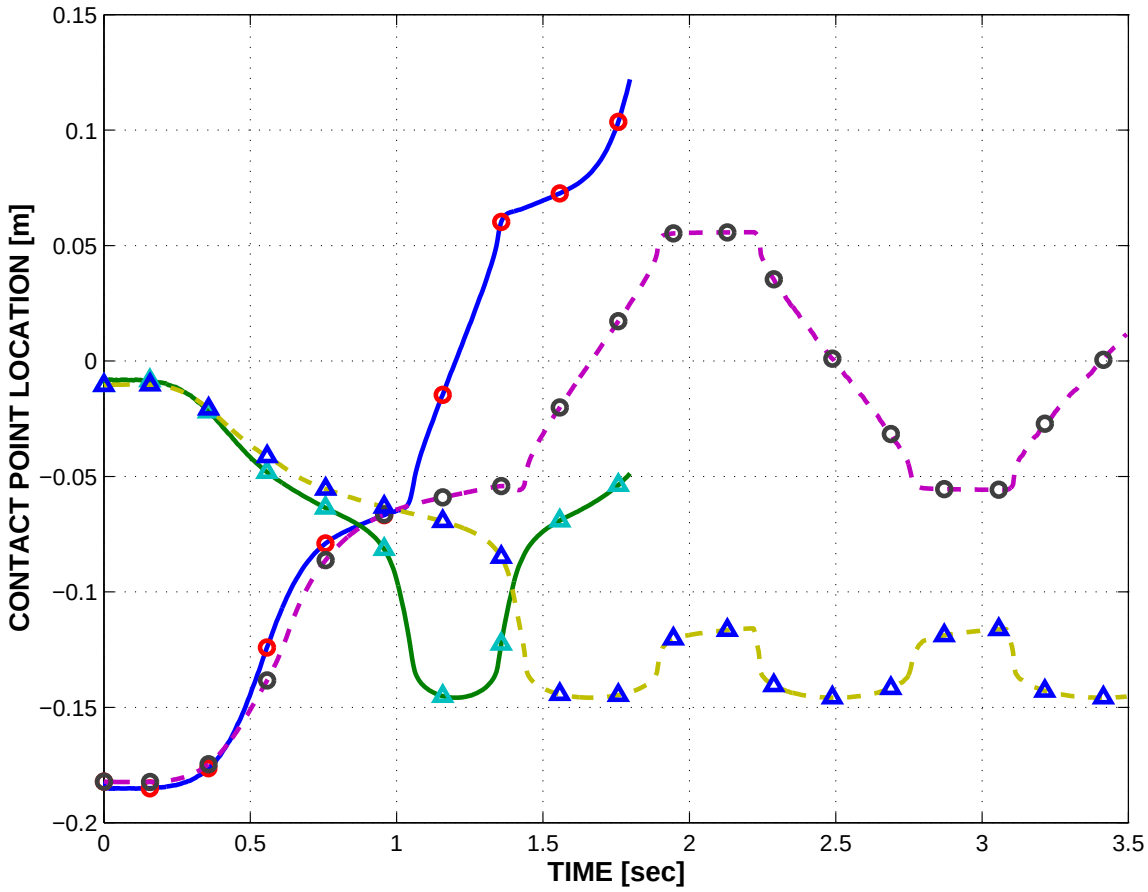

Figure 5: Time history of the contact point x_1 ($\circ$) and x_2 ($\triangle$) position components. *Case 0:* solid line; *case 1:* dashed line.

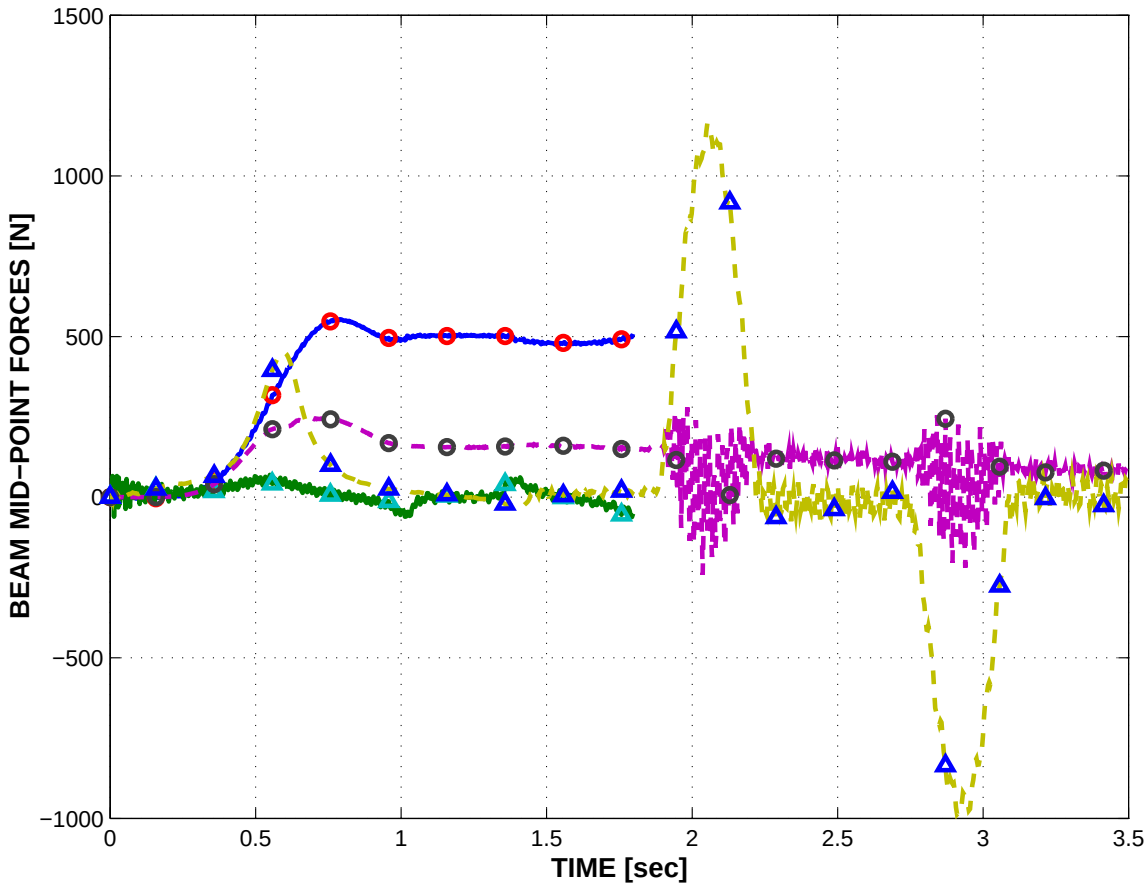

Figure 6: Time history of the beam mid-point axial force (∘) and shearing force (△). *Case 0:* solid line; *case 1:* dashed line.

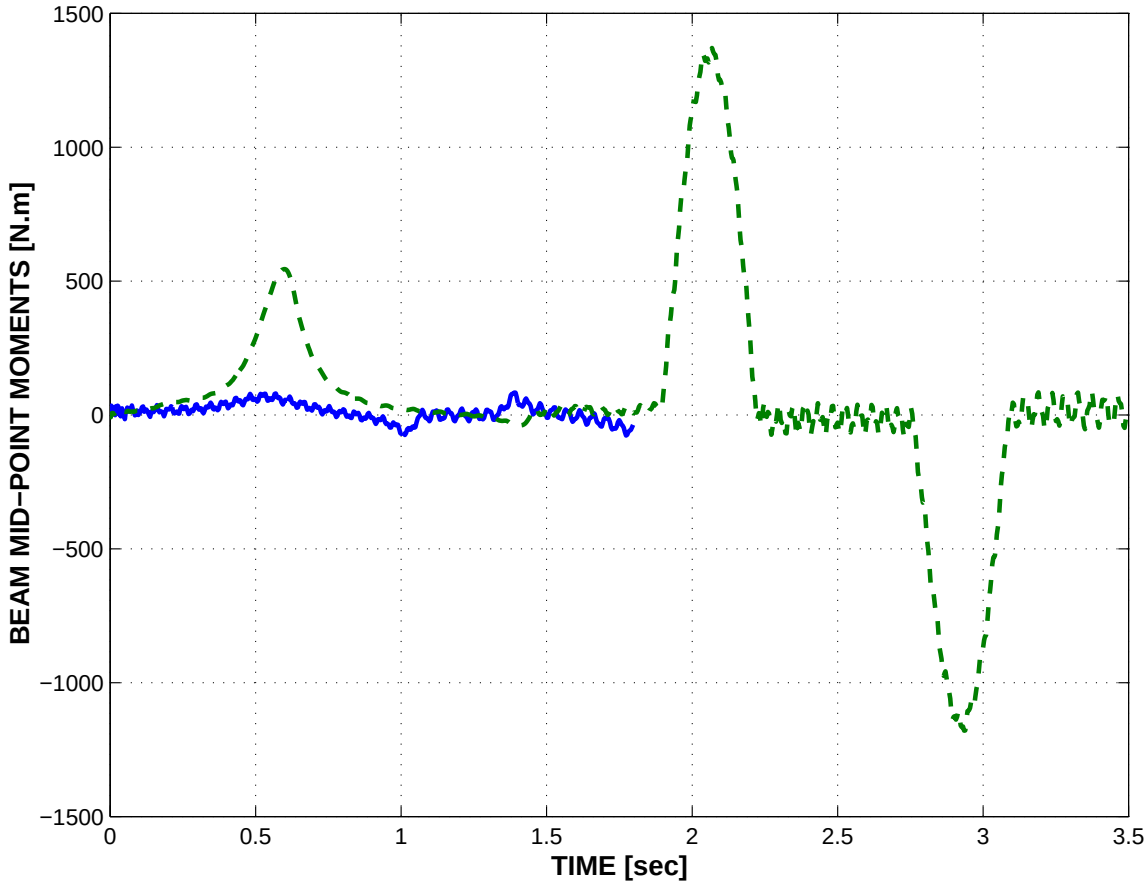

Figure 7: Time history of the beam mid-point bending moment. *Case 0:* solid line; *case 1:* dashed line.

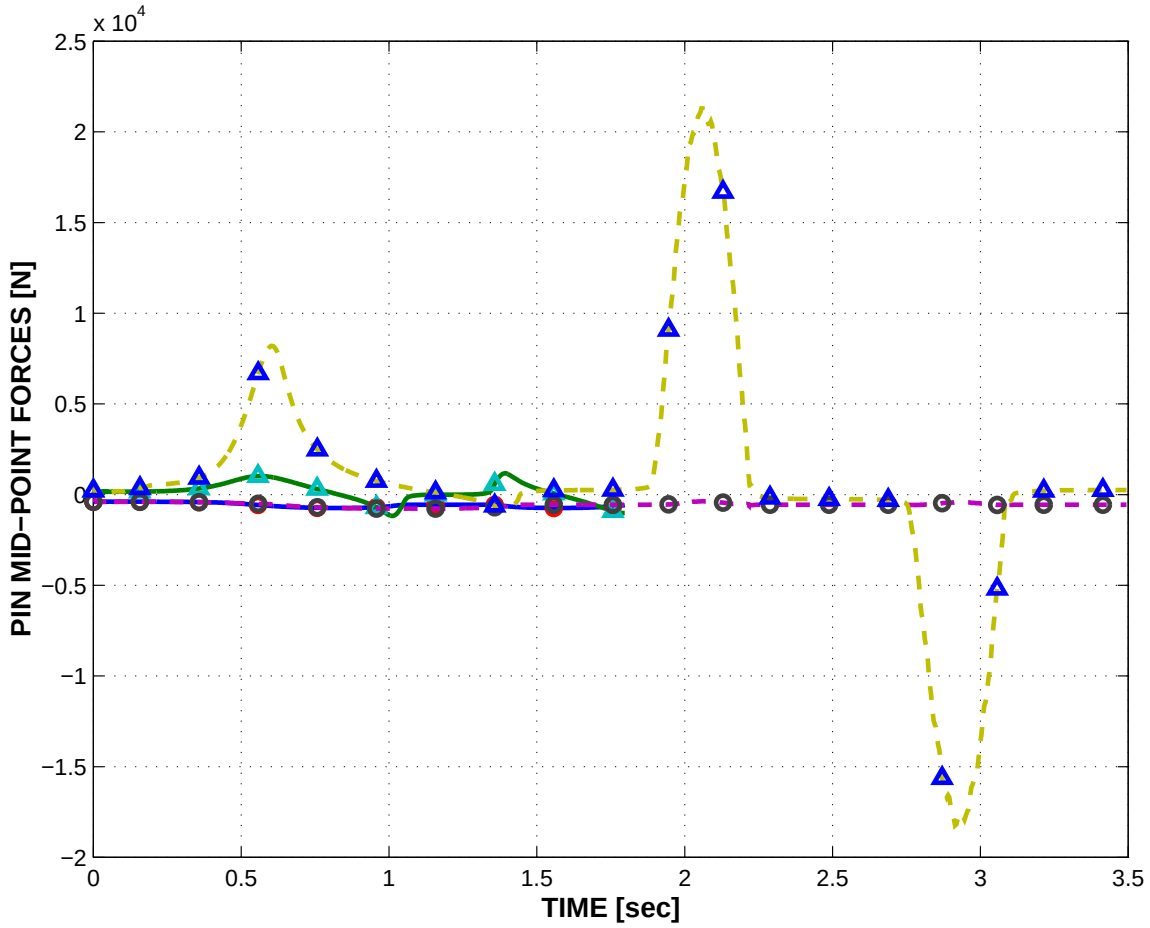

Figure 8: Time history of the pin mid-point axial force (∘) and shearing force (△). *Case 0:* solid line; *case 1:* dashed line.

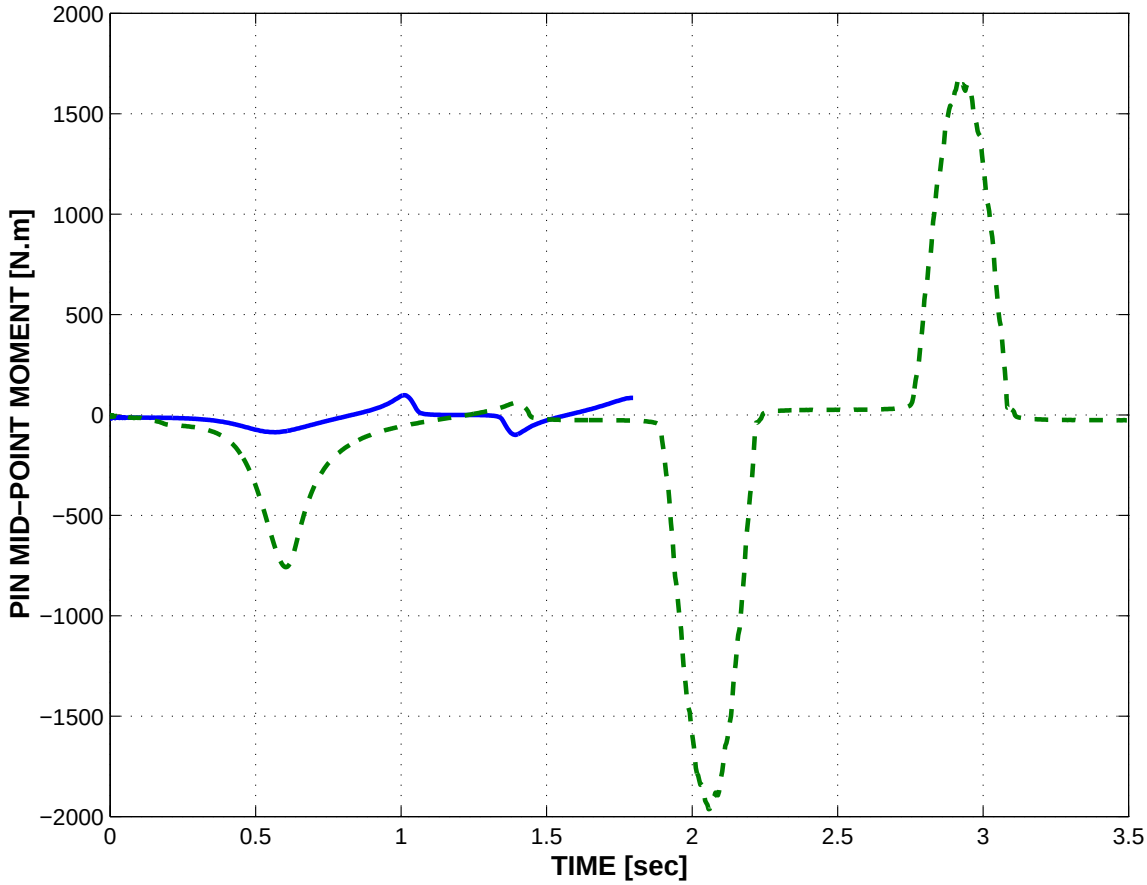

Figure 9: Time history of the pin mid-point bending moment. *Case 0:* solid line; *case 1:* dashed line.

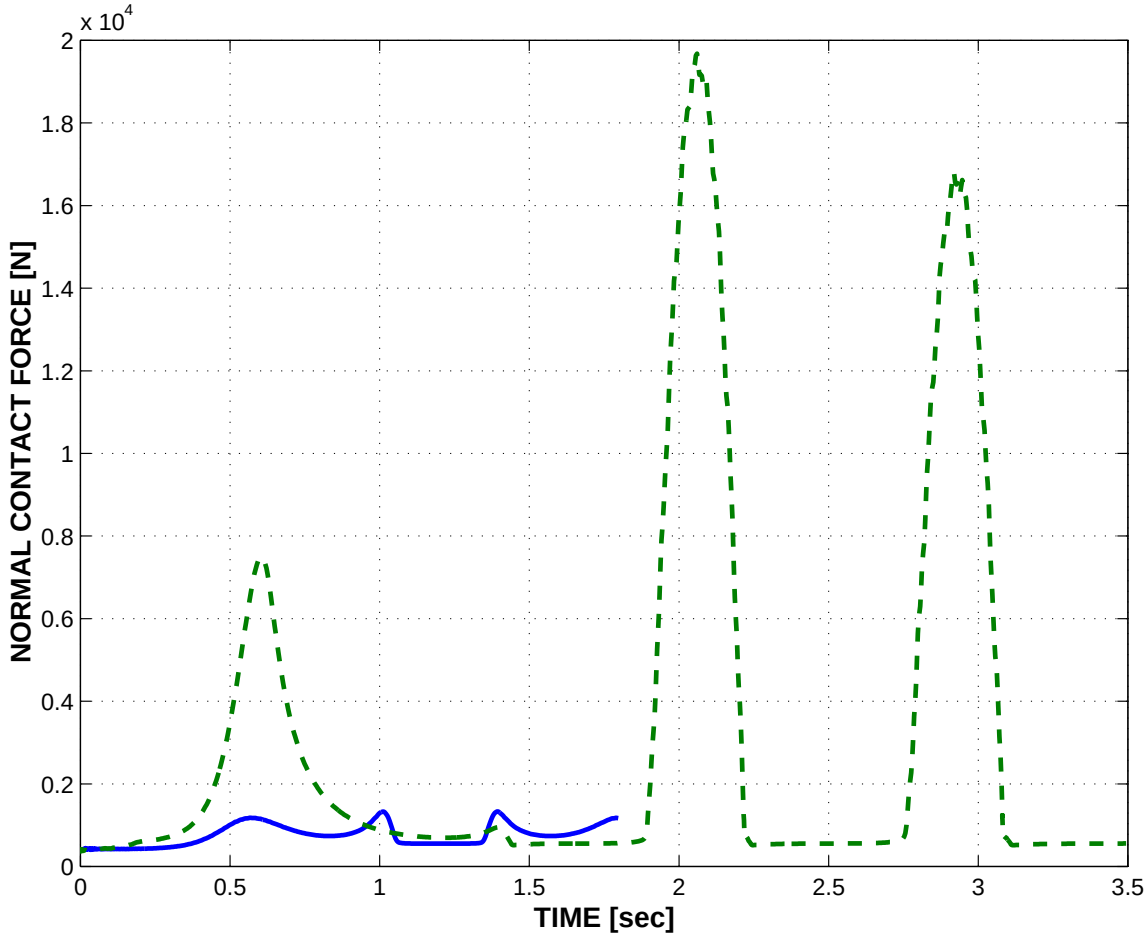

Figure 10: Time history of the normal contact force. *Case 0:* solid line; *case 1:* dashed line.

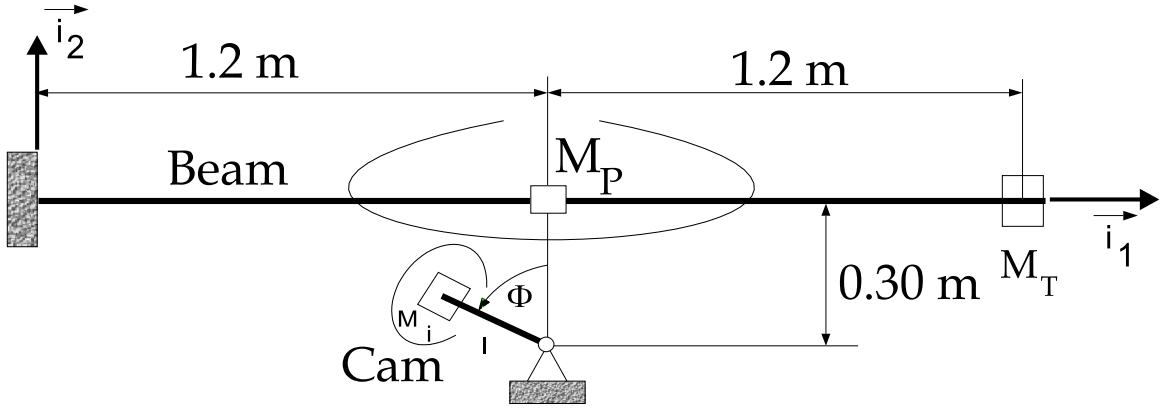

Figure 11: Configuration of the cam and beam.

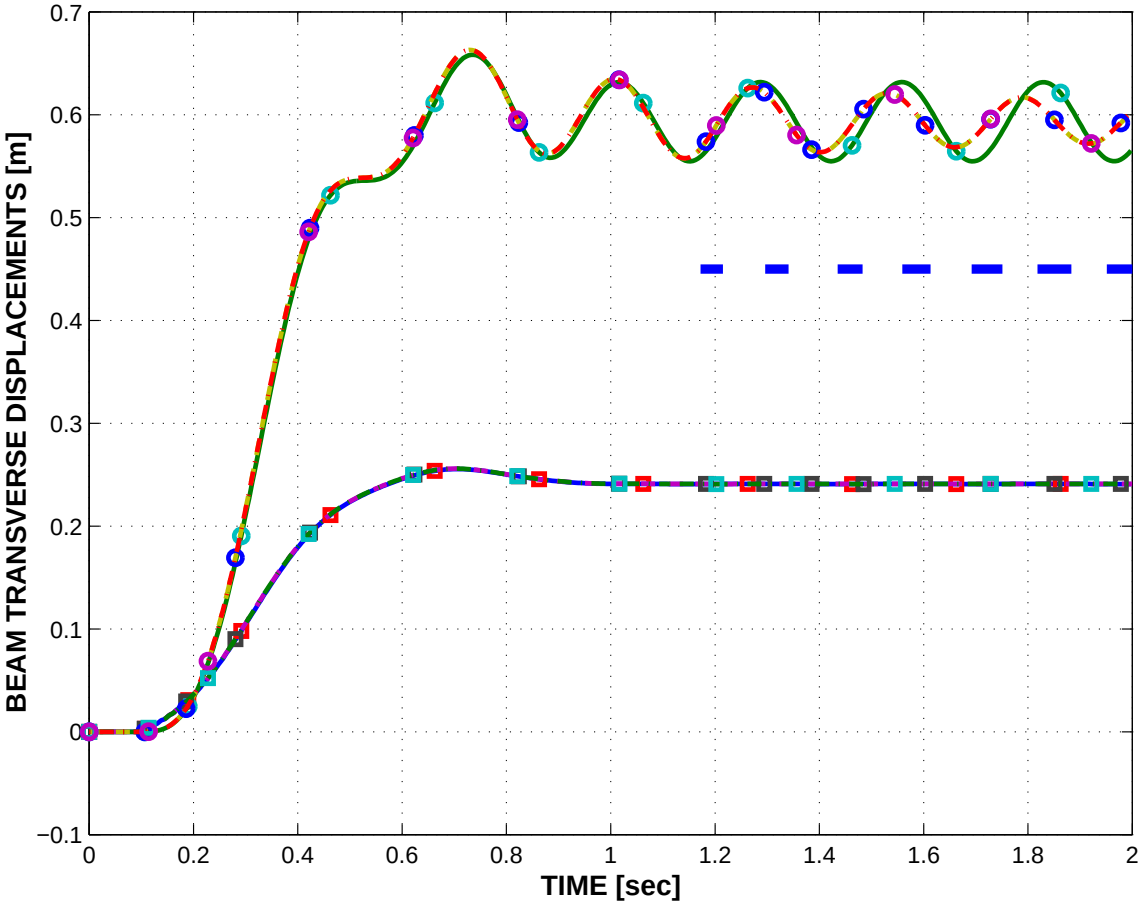

Figure 12: Time history of tip (○) and mid-point (□) transverse displacements. *Case 0:* solid line; *case 1:* dashed line; *case 2:* dash-dotted line.

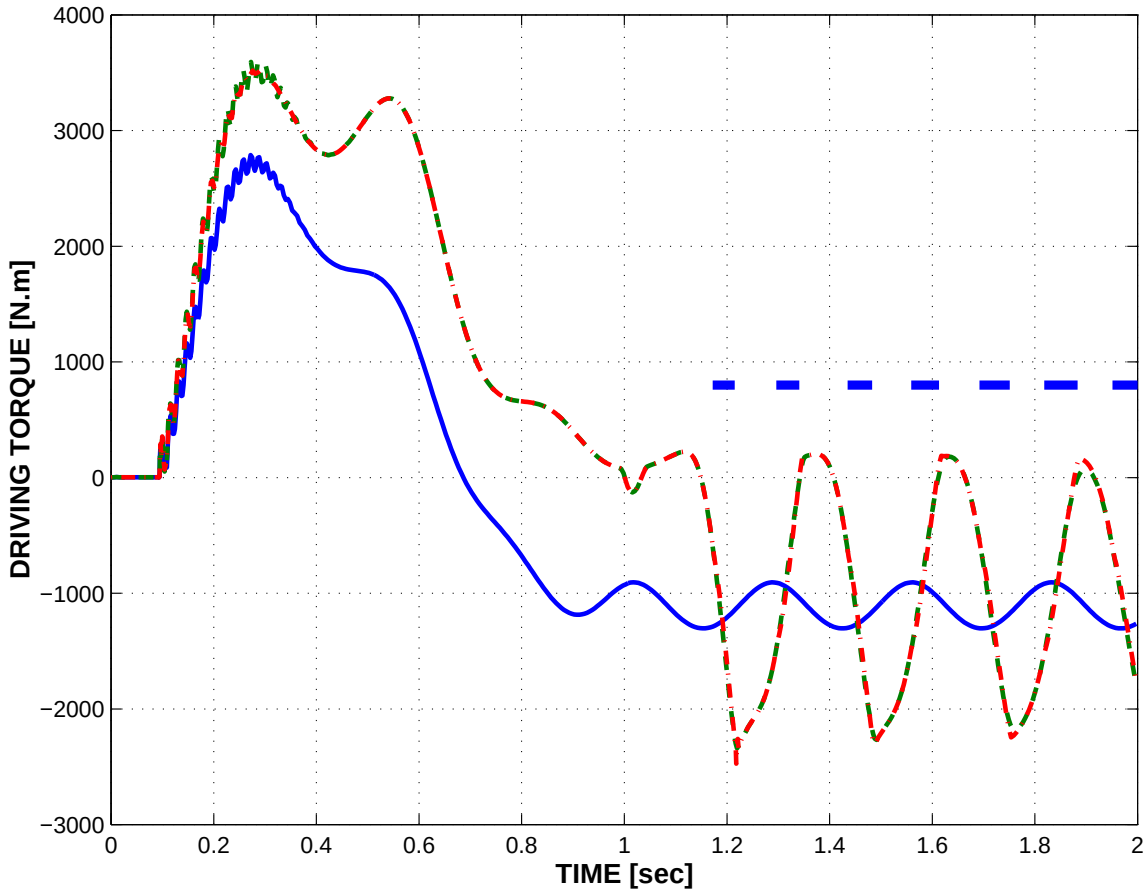

Figure 13: Time history of the driving torque. *Case 0:* solid line; *case 1:* dashed line; *case 2:* dash-dotted line.

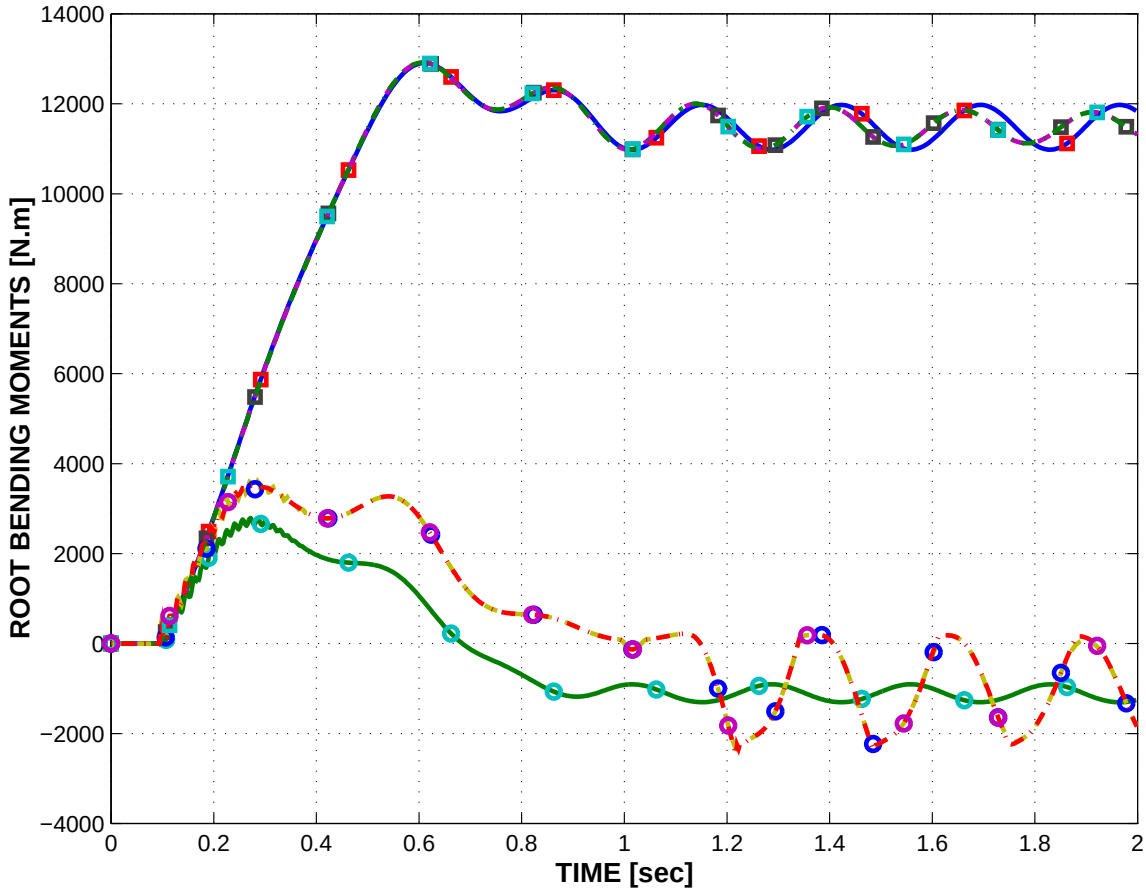

Figure 14: Time history of the root bending moments in the beam (□) and cam (○). *Case 0:* solid line; *case 1:* dashed line; *case 2:* dash-dotted line.

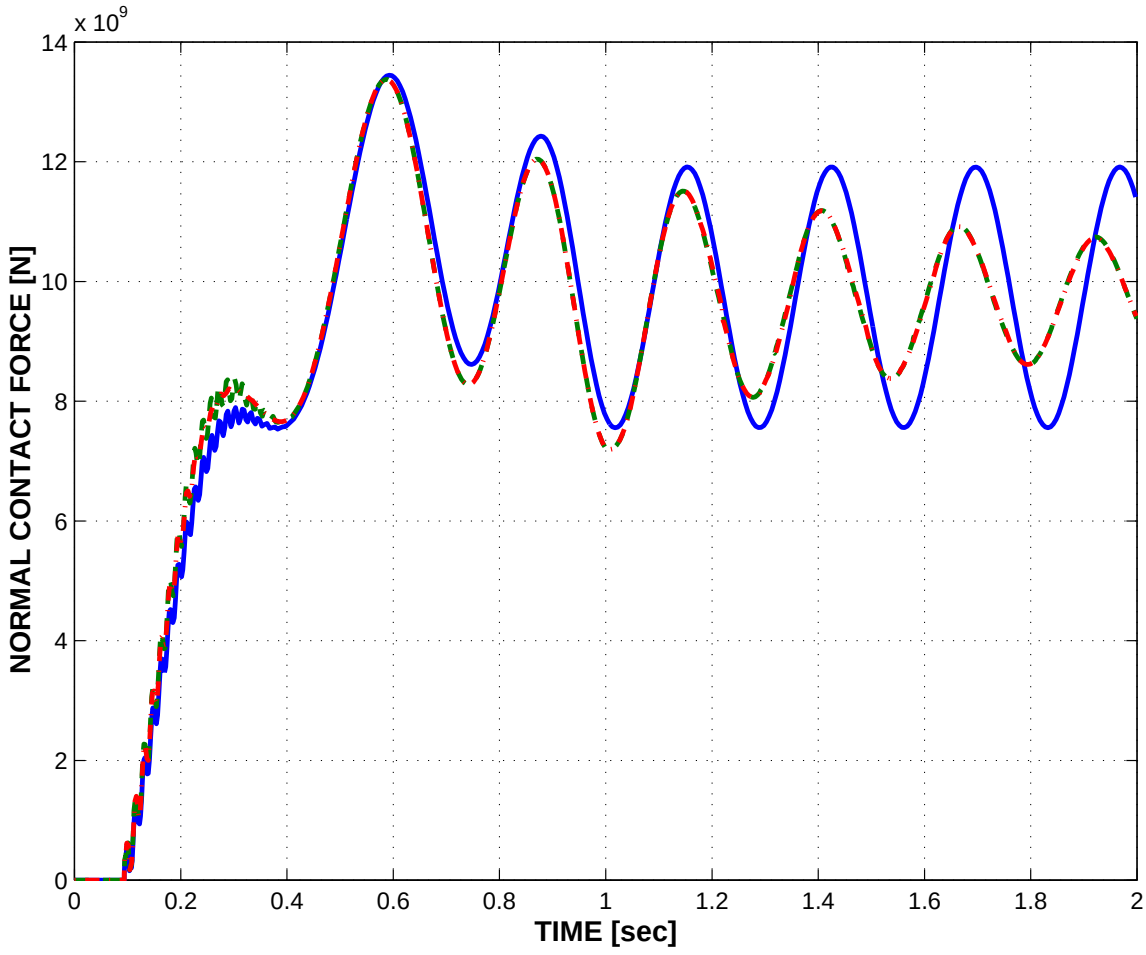

Figure 15: Time history of the normal contact force. *Case 0:* solid line; *case 1:* dashed line; *case 2:* dash-dotted line.

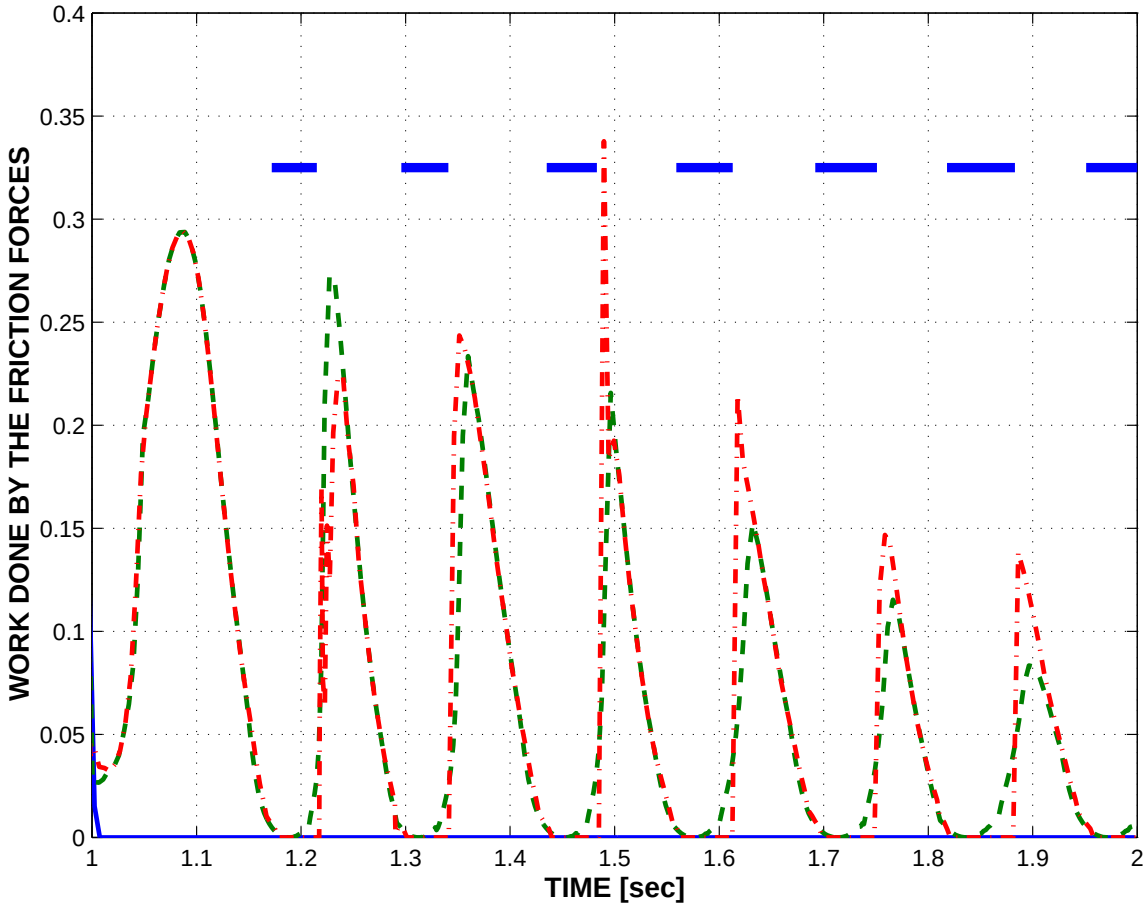

Figure 16: Time history of the work done by the friction forces. *Case 0:* solid line; *case 1:* dashed line; *case 2:* dash-dotted line.

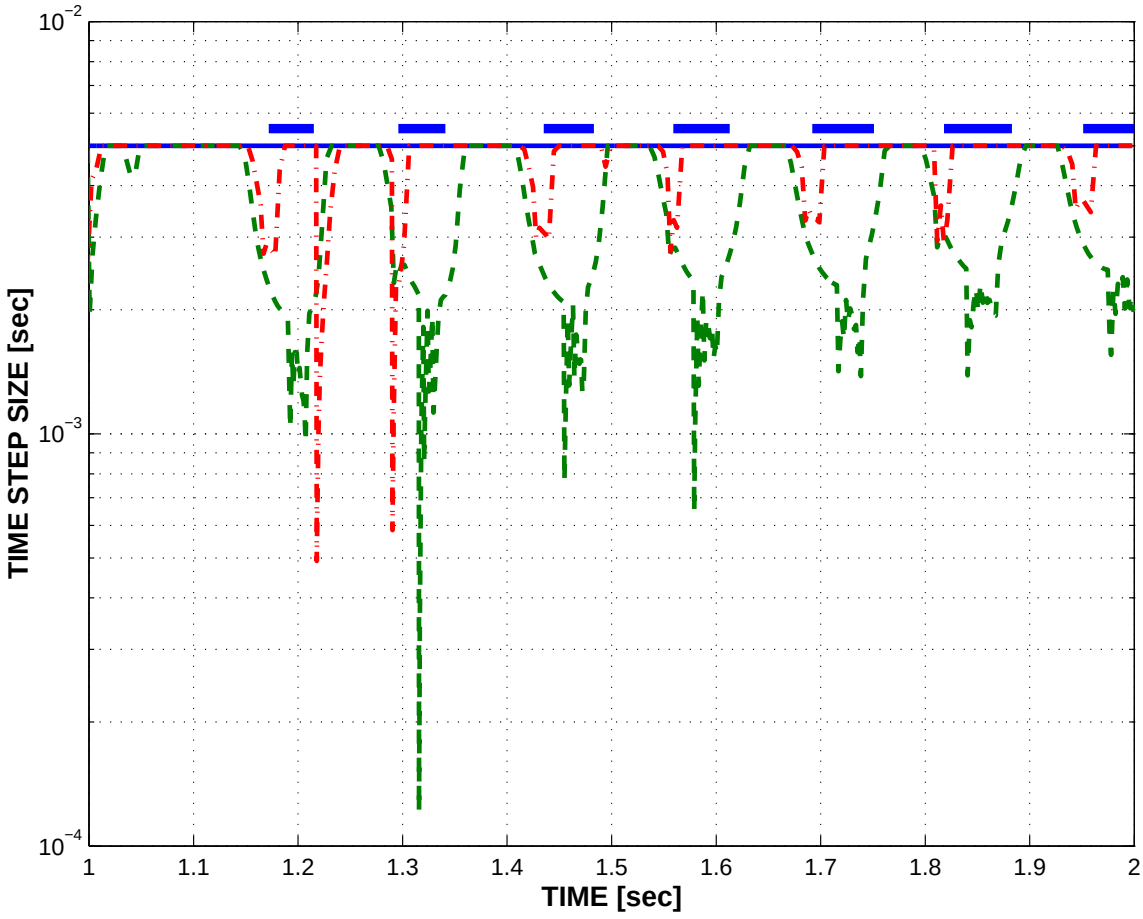

Figure 17: Time history of the time step size. *Case 0:* solid line; *case 1:* dashed line; *case 2:* dash-dotted line.

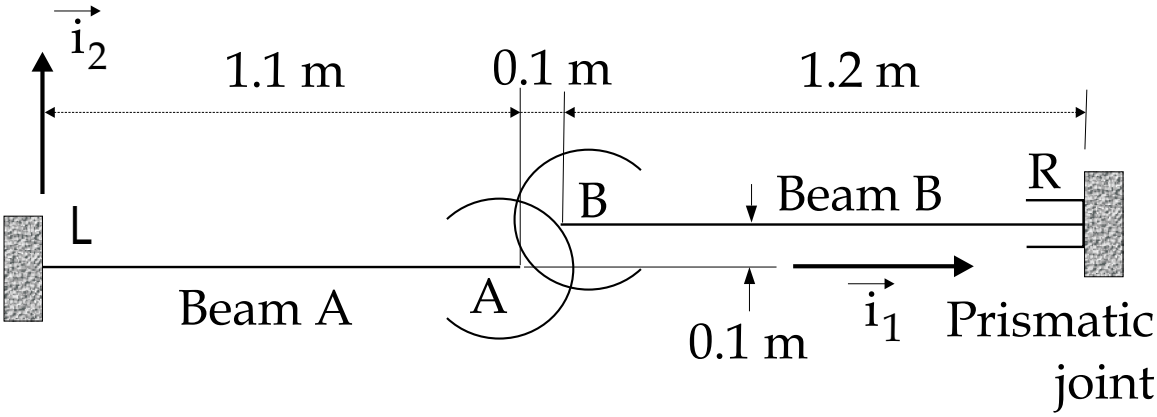

Figure 18: Cam contact with rolling: configuration of the problem.

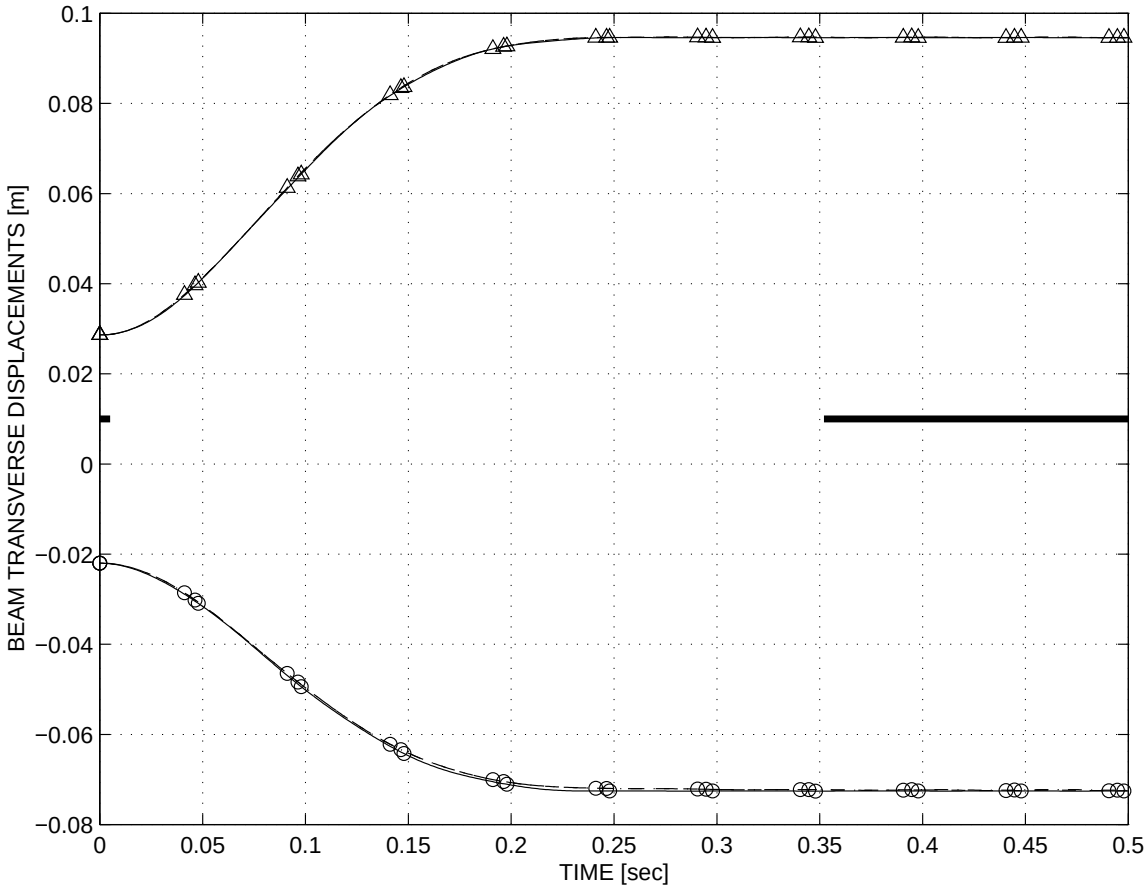

Figure 19: Time history of *beam A* (○) and *beam B* (△) tip displacements. *Case 0:* solid line; *case 1:* dashed line; *case 2:* dash-dotted line.

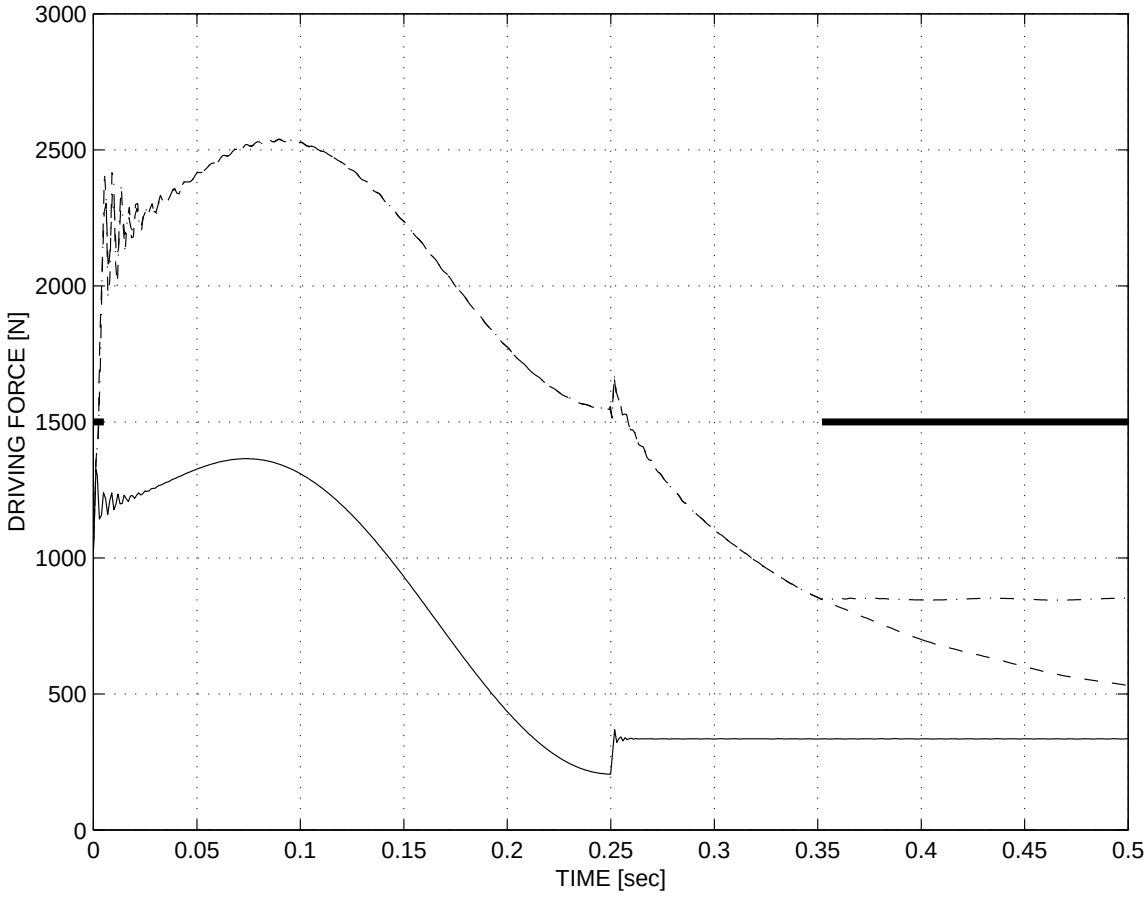

Figure 20: Time history of the driving force. *Case 0:* solid line; *case 1:* dashed line; *case 2:* dash-dotted line.

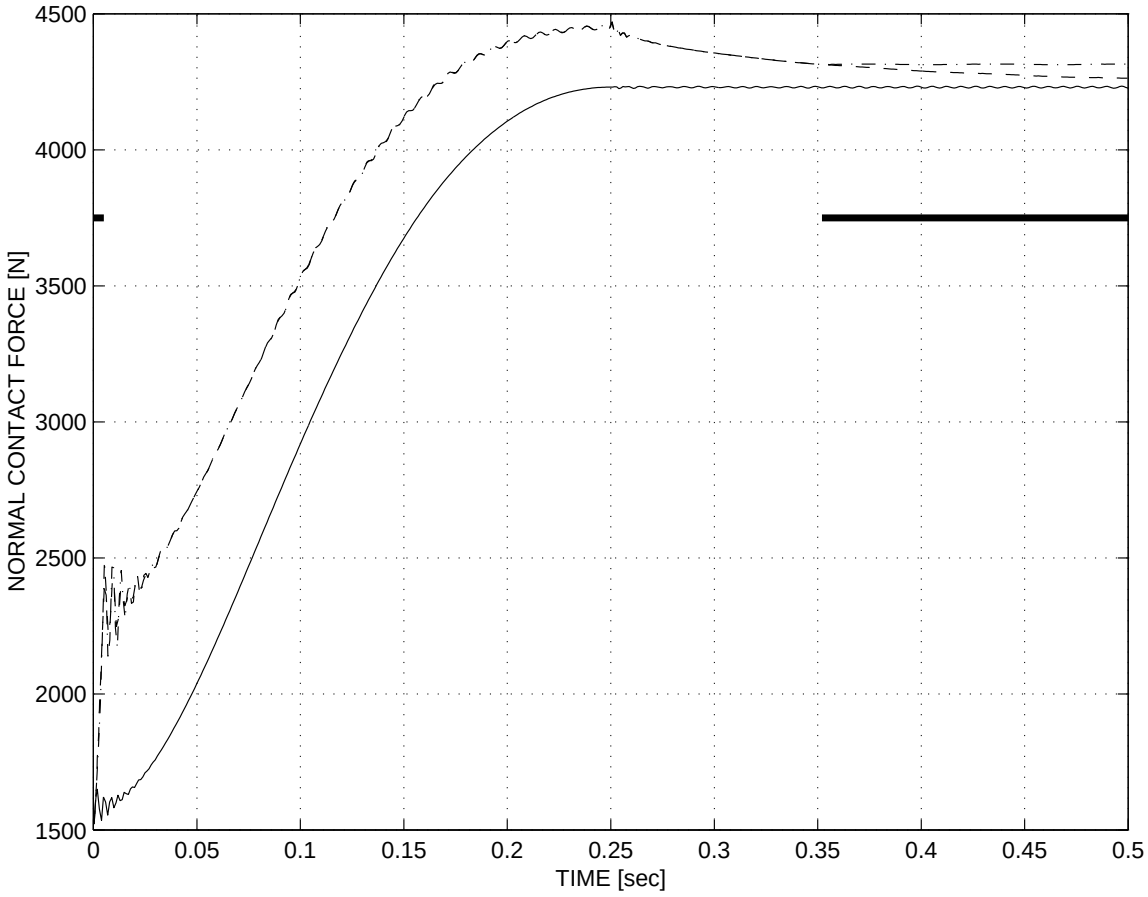

Figure 21: Time history of the normal contact force. *Case 0:* solid line; *case 1:* dashed line; *case 2:* dash-dotted line.

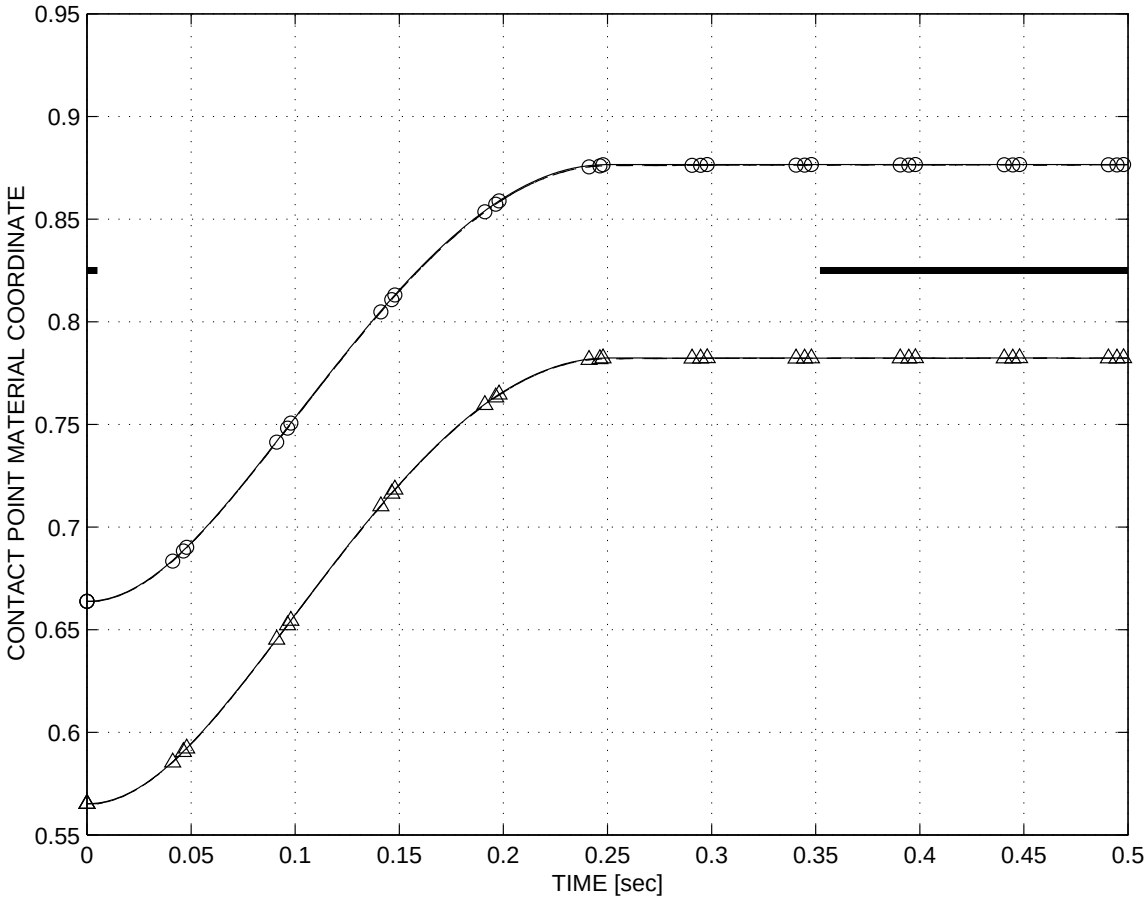

Figure 22: Time history of the point of contact material coordinate on *body A* ($\circ$) and *body B* ($\triangle$). Note: for clarity of the picture, the material coordinate for *body B* was shifted down by 0.1. *Case 0:* solid line; *case 1:* dashed line; *case 2:* dash-dotted line.

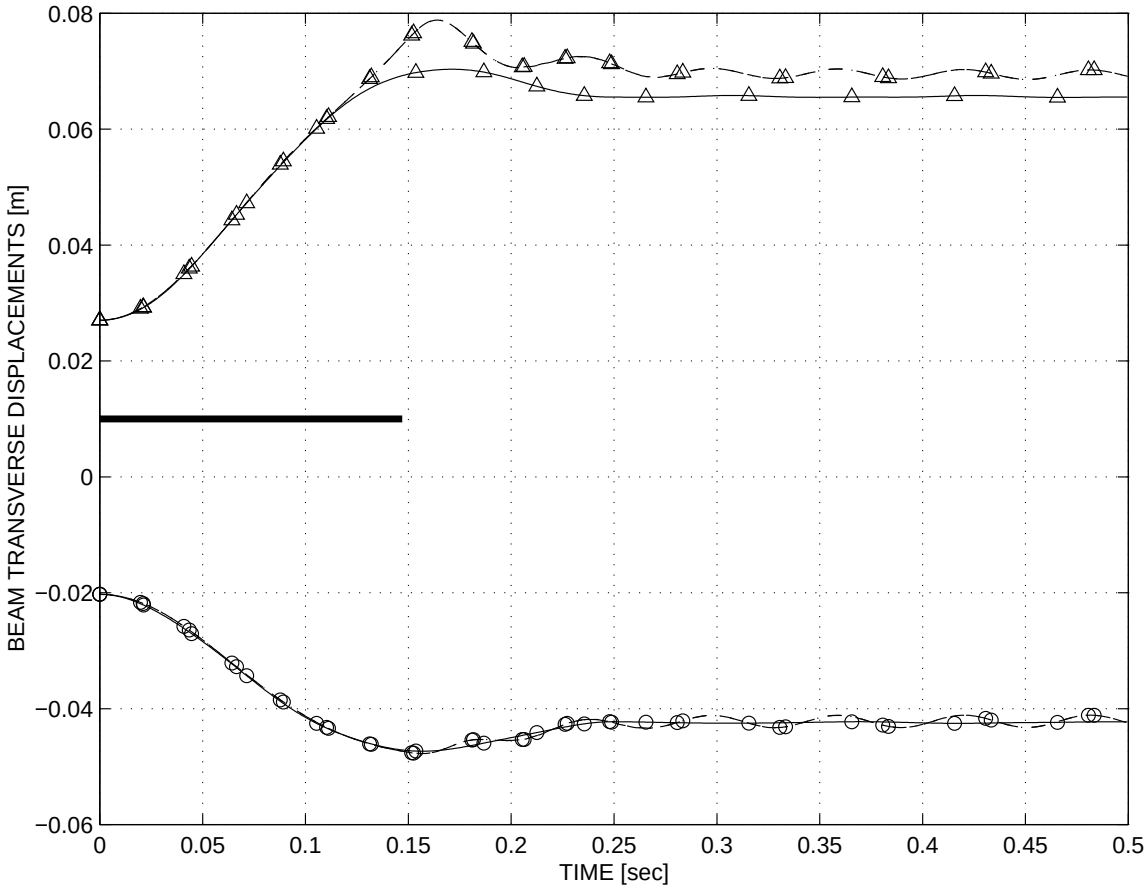

Figure 23: Time history of *beam A* ($\circ$) and *beam B* ($\triangle$) tip displacements. *Case 0:* solid line; *case 1:* dashed line; *case 2:* dash-dotted line.

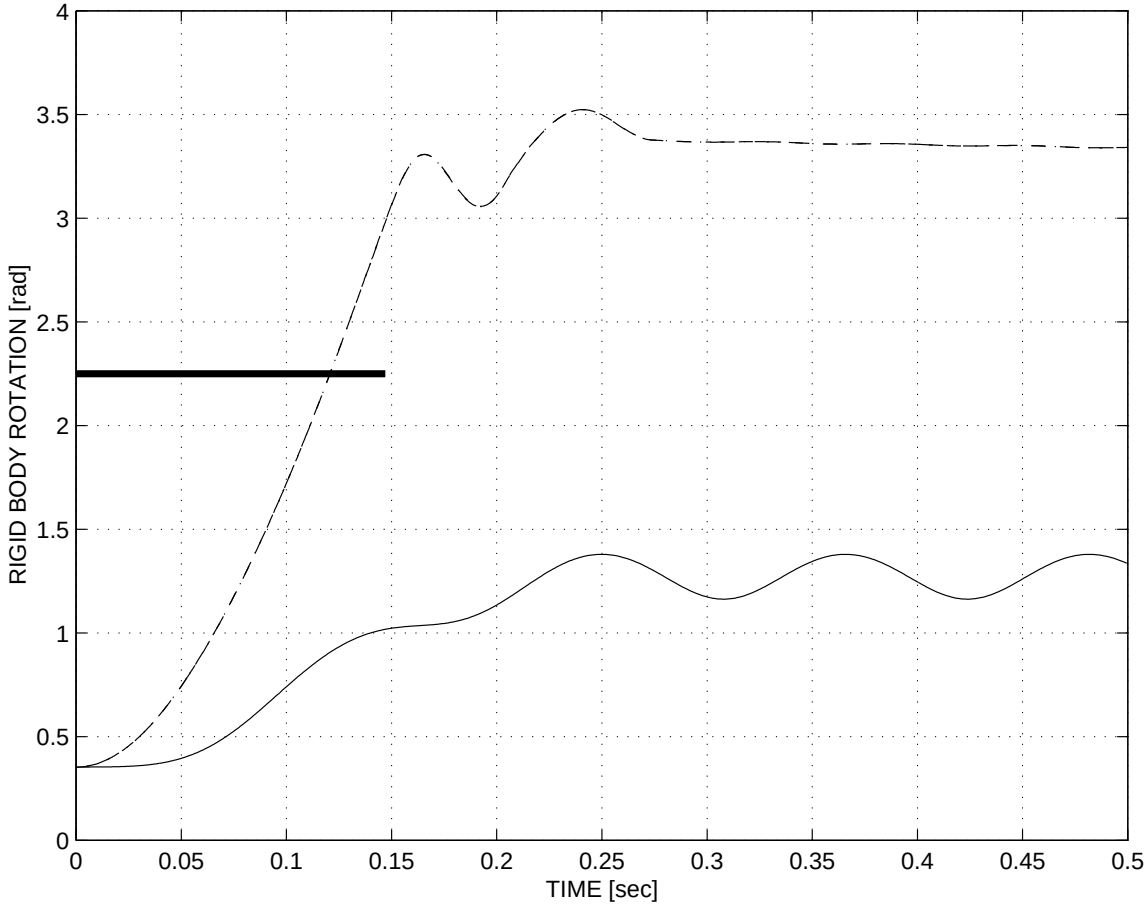

Figure 24: Time history of the rotation of *body B*. *Case 0:* solid line; *case 1:* dashed line; *case 2:* dash-dotted line.

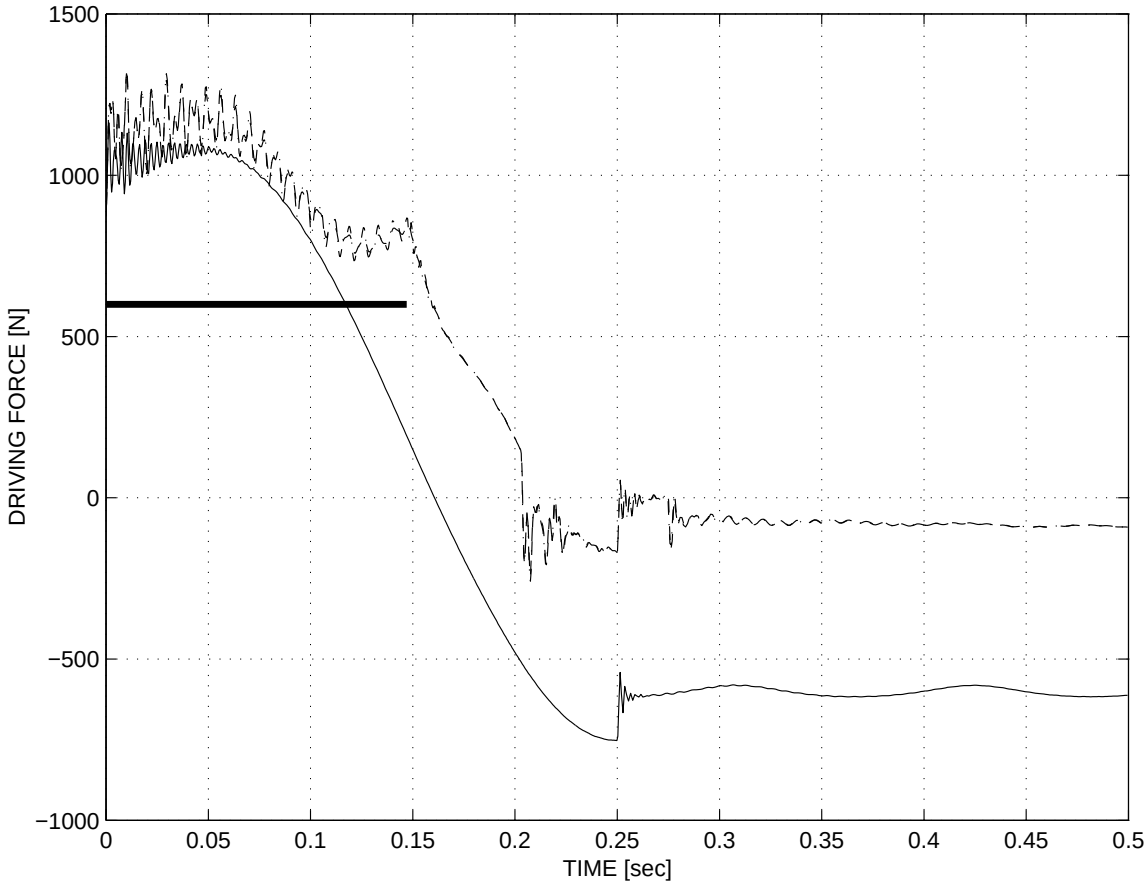

Figure 25: Time history of the driving force. *Case 0:* solid line; *case 1:* dashed line; *case 2:* dash-dotted line.

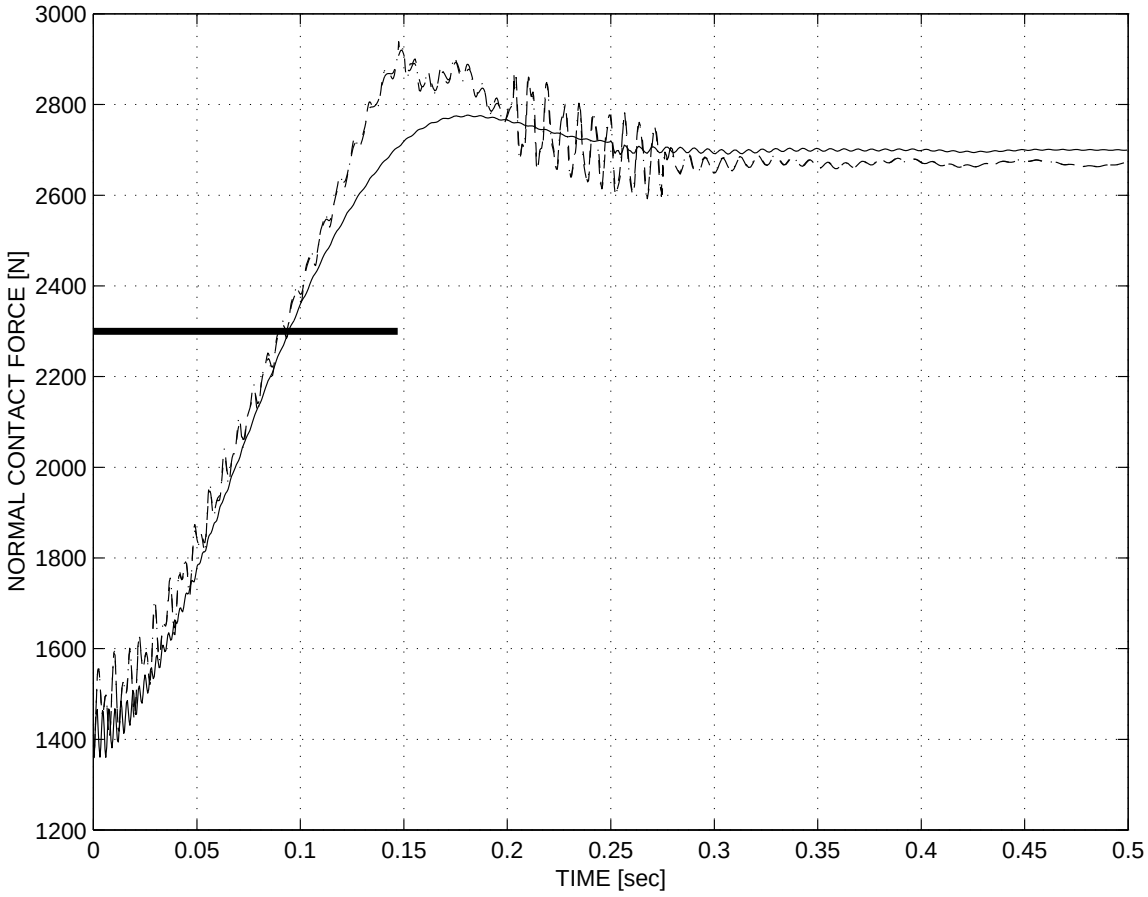

Figure 26: Time history of the normal contact force. *Case 0:* solid line; *case 1:* dashed line; *case 2:* dash-dotted line.

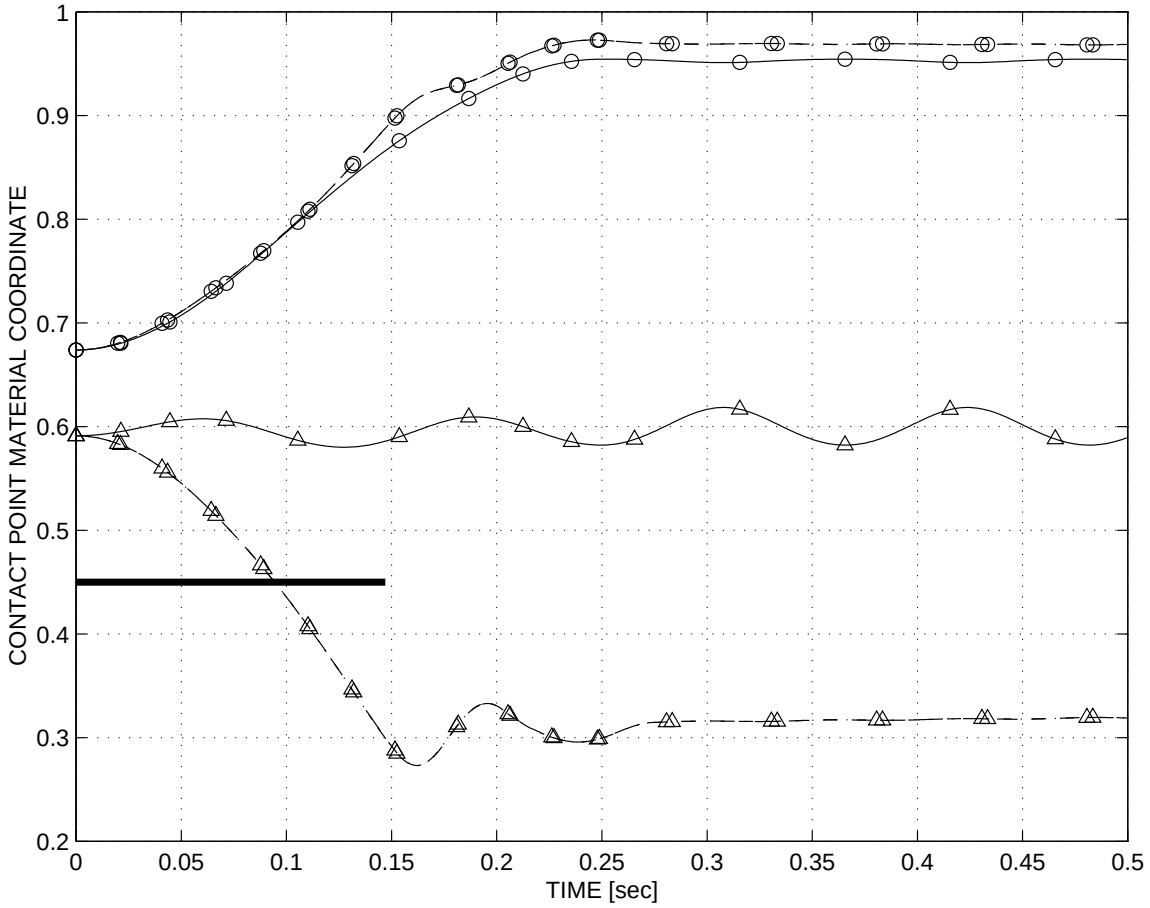

Figure 27: Time history of the point of contact material coordinate on *body A* ($\circ$) and *body B* ($\triangle$). *Case 0:* solid line; *case 1:* dashed line; *case 2:* dash-dotted line.